



university of
 groningen

faculty of mathematics
 and natural sciences

astronomy

UNIVERSITY OF GRONINGEN

KAPTEYN ASTRONOMICAL INSTITUTE

**Kinematics of the dwarf spheroidal galaxies Draco
 and Ursa Minor**

MSc Thesis in Astronomy

by

JOHANNA HARTKE

Groningen, August 14, 2015

SUPERVISORS

Prof. Dr. Eline Tolstoy

Dr. Shoko Jin

Dr. Maarten Breddels

SECOND READER

Prof. Dr. Scott Trager

Abstract

The aim of this thesis is to study the kinematics of the Local Group dwarf spheroidal galaxies Ursa Minor and Draco. These two galaxies are an interesting pair to study, since they are similar in terms of mass, extent, and distance. However, while Draco appears to have a perfect, undisturbed stellar distribution, Ursa Minor shows signs of tidal disturbance. We use new optical spectroscopy of individual red giant branch stars from the AF2-WYFFOS fiber spectrograph on the William Herschel Telescope. We observed several hundred stars in the CaII triplet region. The data have been pipeline-processed at CASU in Cambridge using prototype WEAVE processing. We combine our dataset of Draco with data published by Walker, Olszewski & Mateo (2015) and apply orbit-based Schwarzschild modeling to the velocity data in order to constrain the dwarf spheroidal's (dark) matter distribution. We are able to determine the dark matter halo mass distribution for a NFW and a cored profile.

Contents

1	Introduction	4
1.1	Galaxy Formation	5
1.2	Local Group dSph galaxies	6
1.2.1	Draco	7
1.2.2	Ursa Minor	8
1.3	Dynamical modeling	8
1.3.1	Early attempts to model dSphs	8
1.3.2	Jeans modeling	9
1.3.3	Schwarzschild modeling	10
1.4	Outline of this thesis	11
2	Data	12
2.1	Observations	12
2.2	Results	13
2.2.1	Velocity distribution and membership	13
2.2.2	Metallicity distribution	14
2.3	Literature data	16
3	Schwarzschild modeling	18
3.1	The method	18
3.1.1	Density distribution and model parameters	19
3.1.2	Orbit integration	21
3.1.3	Observables	21
3.1.4	Finding a solution	24
3.2	Testing the method using a Sculptor-like mock galaxy	25
4	Schwarzschild modeling of the Draco dSph galaxy	27
4.1	Setting up the modeling	27
4.1.1	Model parameters	27
4.1.2	Binning	28
4.2	Results	31
4.2.1	WHT data	31

4.2.2	WOM15 data	32
4.2.3	Comparison	34
5	Discussion and Conclusion	40
5.1	Outlook	41
A	Jeans modeling	56

Chapter 1

Introduction

Dwarf galaxies are, as the name suggests, small stellar systems. In this context, small refers to both the system's diameter as well as to its luminosity. The closest dwarf galaxies that can be observed with the naked eye (from the southern hemisphere), are the Small and Large Magellanic Clouds and they are a rather large example of this class. Dwarf galaxies are found in all environments including groups and clusters of galaxies. In these populated environments, dwarf galaxies are often satellites of a larger galaxy.

Dwarf galaxies are classified by their morphology. One distinguishes between dwarf irregular (dIrr), dwarf elliptical (dE), and dwarf spheroidal (dSph) galaxies. The latter two types do not show signs of recent star formation, while star formation is still ongoing in dIrrs, which is the reason why dE and dSph galaxies consist of an old stellar population, while dIrr galaxies also contain young stars.

Even though we are surrounded by a large number of dSphs in the Local Group, the first dSph galaxies were only discovered towards the middle of the 20th century, due to their faintness. The first Local Group dSphs were discovered by Shapley (1938), and were named after the constellations they were observed in, Sculptor and Fornax.

It is believed that dSph galaxies are among the most dark-matter-dominated galaxies in the Local Group and therefore provide an ideal testing ground for details of Λ CDM cosmological models. As the name suggests, they are among the smallest type of galaxies we know of. From their kinematics one can infer a high mass-to-light ratio (M/L), which indicates that they contain a large amount of dark matter. The first ideas about the evidence for the existence of dark matter were made by the astronomers Oort and Zwicky in the first half of the twentieth century, and were based on kinematic studies. Zwicky (1937) compared the luminous mass to the total mass in the Coma cluster, the latter being inferred from the motions of galaxies in the cluster. He inferred a much larger total mass than is visible and thus suggested unseen, dark matter (DM) as an explanation for this discrepancy. According to recent results from the Planck mission, we now know that our Universe consists of 68.25% of dark energy, 4.90% baryonic (visible) matter, and 26.71% dark matter (Planck Collaboration 2014).

1.1 Galaxy Formation

Dark matter plays an important role in structure formation. At the moment, a cold dark matter (CDM) dominated Universe with a cosmological constant (Λ CDM) is favored, since it can explain the observed large scale properties of galaxy distributions. In Λ CDM, structure forms hierarchically (White & Rees, 1978; Peebles, 1982). CDM consists of massive, non-relativistic (cold) particles, whose interaction is even weaker than the weak interaction. Their low velocities, with a dispersion that is insignificant with respect to the Hubble flow, allows for a collapse of structure on all scales.

Structure formation originates in small adiabatic density fluctuations, which, on the smallest scales, can be observed in the cosmic microwave background. As gravity is the driving force in structure formation, overdensities become denser with time, attracting more matter from underdense regions, which in turn get even less dense. Once an overdense region reaches a critical density, it starts to collapse, forming a small halo. These are the building blocks of larger structures, which are formed via mergers and accretion. Small objects like dSphs are expected to have formed before bigger galaxies, such as the the Milky Way (MW). This makes dSphs particularly interesting to study. They are potentially the building blocks of galaxies like our own, but also provide insights into structure formation in the early Universe.

While Λ CDM is in good agreement with observed large-scale structures, problems arise on the scales of individual galaxies. By studying cosmological N-body simulations, Navarro, Frenk & White (1996, 1997) showed that objects that form in a Λ CDM cosmology follow a universal density profile, called the NFW profile, on all scales, from clusters of galaxies to dwarf galaxies. However, the profile does not fit some low-surface-brightness galaxies, which favor a cored rather than a cusped DM distribution (e.g., de Blok, 2010). This might be due to more complicated processes involving the baryonic component, such as feedback processes from star formation. For small systems like dSph galaxies, the energy released by a supernova event can be comparable to the system's binding energy. Therefore feedback, from explosions like supernovae should be able to transform a cuspy halo into a cored one in more massive systems (e.g., Navarro, Eke & Frenk, 1996). However, it is not yet clear whether this is also the case in dSphs (Peñarrubia et al., 2012), since their star formation rate is much lower than that in more massive galaxies.

Typical DM simulations do not contain baryons and thus cannot account for the feedback mechanisms affecting the baryonic component. Comparisons between DM-only simulations and observations are thus not completely straightforward as one cannot directly link a luminous (satellite) galaxy to a corresponding DM (sub-) halo. Therefore, on the theoretical side, it is important to incorporate baryonic effects in semi-analytic or hydrodynamic simulations of (dSph) galaxies (e.g., Cole et al., 1994; Somerville & Primack, 1999; Benson et al., 2002a; Benson et al., 2002b; Salvadori, Schneider & Ferrara, 2007; De Lucia & Helmi, 2008; Revaz et al., 2009; Revaz & Jablonka, 2012; Starkeburg et al.,

2013). On the observational side, it remains important to obtain accurate total mass estimates of dSphs.

Another issue that arises at the mass scale of dSphs is the missing satellite problem. Λ CDM models predict that galaxies like the MW should be surrounded by 100-1000 DM subhalos of the mass of dSph galaxies (Klypin et al., 1999; Moore et al., 1999). At the beginning of this century, only 11 MW satellite galaxies had been identified. With the Sloan Digital Sky Survey, more than a dozen faint MW satellites have been discovered in the last decade (Willman et al., 2005b; Willman et al., 2005a; Zucker et al., 2006a; Zucker et al., 2006b; Belokurov et al., 2006; Belokurov et al., 2007; Walsh, Jerjen & Willman, 2007). The faintest of these systems are also known under the name of ultra-faint dwarfs and new systems are still being discovered (e.g., Koposov et al., 2015).

1.2 Local Group dSph galaxies

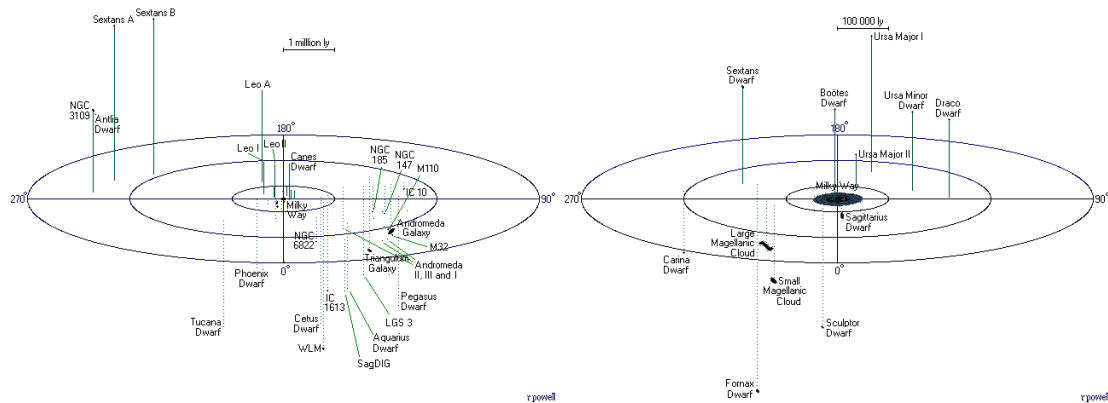


Figure 1.1: Galaxies in the Local Group (left) and a zoom-in of the satellite-galaxy system of the MW (right, Powell (2015)).

Throughout the universe, galaxies are typically not distributed uniformly, but found in groups or clusters consisting of multiple galaxies. The smaller associations are called groups and the bigger ones clusters. The Local Group consists of more than 80 galaxies within a radius of about 1 Mpc (McConnachie, 2012, Table 1, updated 2014). The three biggest galaxies are spirals: the MW, the Andromeda galaxy (M31), and the Triangulum galaxy (M33). The MW and M31 are approaching each other and are predicted to eventually merge. As already mentioned, both the MW and M31 are surrounded by many smaller satellite galaxies. Figure 1.1 shows the distribution of galaxies in the Local Group and a zoom-in of the satellite-galaxy system of the Milky Way.

In the Local Group, dSphs are typically found close to the MW (within a radius of 300 kpc), whereas dIrr galaxies are found far from it. This is called the morphology-density relation (Einasto et al., 1974; van den Bergh, 1999). While dSphs are pressure-supported and devoid of gas, dIrrs are rotation-supported and contain gas. The transformation of a

rotation-supported system (dIrr) to a pressure-supported one (dSph) may be possible via tidal stirring due to the host galaxy (Mayer et al., 2001; Mayer et al., 2006).

Due to their proximity, the satellites of the MW (and M31) have been excellent targets for resolved stellar population studies (Baade, 1944a,b). The study of a galaxy's color-magnitude diagram (CMD) allow us to accurately determine its star formation history. The dSph galaxies in the Local Group mostly consist of older stellar populations, which are also found in late-type galaxies. However, the star formation in dSphs ceased sometimes millions of years ago, sometimes billions of years ago (e.g., Tolstoy, Hill & Tosi, 2009; Weisz et al., 2011; Weisz et al., 2014).

An extensive review of the structural properties of the Local Group dwarf galaxies has been published by Mateo (1998) and is still used for reference. In this thesis, we are going to focus on two northern dSphs, Draco and Ursa Minor, which have been named after the constellations in which they are found. They were both discovered by A. G. Wilson during the National Geographic Society's Palomar Observatory Sky Survey in 1954 (Wilson, 1955). While Draco appears to have a perfect, undisturbed stellar distribution, Ursa Minor shows signs of tidal disturbance. The two galaxies are otherwise similar in terms of mass, extent, distance, and position on the sky, making them an interesting pair to analyze using the same methods.

1.2.1 Draco



Figure 1.2: *Image of the Draco dSph (Moore, 2015).*

Draco is a small, faint, and metal-poor dSph galaxy. Its coordinates are RA $17^{\text{h}}20^{\text{m}}19^{\text{s}}$ and Dec $+57^{\circ}54.8'$ (J2000) and its distance is 82 ± 6 kpc (Grillmair et al., 1998). Its line-of-sight (LOS) optical velocity is -293 ± 2 km/s (Armandroff, Olszewski & Pryor, 1995). One can barely make it out in Figure 1.2. It mainly consists of old, metal-poor stars (Baade & Swope, 1961) and a smaller intermediate-age population (Aaronson, 1983). The first spectroscopic studies revealed a spread in

metallicity (Zinn, 1978), which has been confirmed by high-resolution spectroscopy (Shetrone, Bolte & Stetson, 1998). Draco has ceased star formation long ago and does not show any signs of tidal disruption (e.g., Odenkirchen et al., 2001; Piatek et al., 2002; Dolphin, 2002; Klessen, Grebel & Harbeck, 2003).

Draco has received much attention due to its high velocity dispersion. Since it does not show any signs of tidal interaction with the MW, the dispersion is assumed to be due to a high DM content. Previous studies have inferred M/L well above $100 M_{\odot}/L_{\odot}$ (e.g. Kleyana et al., 2001; Odenkirchen et al., 2001).

1.2.2 Ursa Minor



Figure 1.3: *Image of the Ursa Minor dSph (Binnewies & Pöpsel, 2015).*

Ursa Minor is another faint satellite dSph and shown in Figure 1.3. Its coordinates are RA $15^{\text{h}}09^{\text{m}}11^{\text{s}}$ and Dec $+67^{\circ}12.9'$ (J2000). Its distance is 66 ± 3 kpc (Olszewski & Aaronson, 1985) and its LOS optical velocity is -248 ± 2 km/s (Armandroff, Olszewski & Pryor, 1995). In many of its properties, it is similar to the Draco dSph galaxy, but in contrast to Draco, it shows signs of tidal interaction with the MW (e.g., Hodge & Michie, 1969; Martínez-Delgado et al., 2001). Stellar members

have been detected well beyond the tidal radius and it also shows signs of stellar substructure (e.g., Olszewski & Aaronson, 1985; Irwin & Hatzidimitriou, 1995; Kleyna et al., 1998). Its stellar population is old and metal poor (Canterna & Schommer, 1978; Zinn, 1981; Shetrone, Côté & Sargent, 2001).

1.3 Dynamical modeling

1.3.1 Early attempts to model dSphs

One of the first attempts to determine a dSph's M/L was made by Aaronson (1983). He observed the spectra of three carbon stars in Draco and one in Ursa Minor with the Multiple Mirror Telescope (MMT) Echelle spectrograph. The spectrum of one of the observed Draco stars suggested a binary system. The LOS velocities were determined using velocity templates from galactic carbon stars. Since calculating a velocity dispersion from three measurements is crude, Aaronson instead determined the minimum velocity dispersion allowable by a χ^2 -test at 5% level, which results in $\langle V_r^2 \rangle = (6.5 \text{ km/s})^2$. He used the following relation between mass M and velocity dispersion $\langle V_r^2 \rangle$ for globular clusters by Illingworth (1976)

$$M = 167 r_c \tilde{m} \langle V_r^2 \rangle, \quad (1.1)$$

which is based on the velocity distribution function of King (1966). The object's core radius is denoted with r_c and \tilde{m} is a dimensionless mass parameter, which combines multiple parameters of the King model. Using $r_c = 6.5'$ and $\tilde{m} = 4.1$ results in a M/L of

$$M/L = 0.72 \langle V_r^2 \rangle = 31 M_{\odot}/L_{\odot}. \quad (1.2)$$

This is much larger than the M/L of a typical globular cluster, which is of the order of $3 M_{\odot}/L_{\odot}$. Aaronson’s result went hand in hand with the theoretical findings of Faber & Lin (1983), who derived the masses of dSphs using the tidal limit theory. They assumed that dSphs are tidally limited by the gravitational field of the Milky Way and can be described by truncated cluster models (King, 1962), which results in the following expression for the tidal radius r_t :

$$r_t = d_p \left(\frac{M_{\text{dSph}}}{(3 + e)M_{\text{MW}}} \right)^{1/3}, \quad (1.3)$$

where M_{MW} is the mass of the MW within the perigalactic distance d_p ; M_{dSph} is the mass of the dSph within r_t , and e is the orbital eccentricity. Instead of inferring the mass of the MW from the dSph mass, this formula can be inverted in order to obtain M_{dSph} . Using $r_t = 0.5$ kpc, they obtain a M/L of $13 M_{\odot}/L_{\odot}$, which is consistent with Aaronson’s result within the 95% confidence level. They also concluded that the M/L values of dSphs are roughly one order of magnitude higher than those of globular clusters.

Rood, Page, Kintner & King (1972) introduced an analytic model based on the King model in order to determine the M/L of the Coma Cluster using the system’s projected density distribution. Their formalism was expanded by Richstone & Tremaine (1986) to determine the M/L of spherical stellar systems. The M/L can be written as

$$\frac{M}{L} = \eta \frac{9\sigma_0^2}{2\pi G I_0 R_e}, \quad (1.4)$$

where σ_0 is the central velocity dispersion; I_0 is the central surface brightness; R_e is the half-light radius at which the surface brightness drops to half its central value, and η is a model-dependent dimensionless factor. In almost any spherical system with an isotropic velocity distribution, M/L independent of radius, and a well-defined, flat, central core, η is near unity. King’s method uses equation 1.4 with $\eta = 1$. This method is, for example, applied by Kleyna et al. (2005) to determine the M/L of Ursa Major. However, the authors state that the assumption of a constant M/L independent of radius does not hold for a dSph with a DM halo. Clearly, a different approach that does not require such an assumption to be made would be preferred.

1.3.2 Jeans modeling

Jeans modeling is another technique for modeling the line-of-sight velocity distribution (LOSVD) of galaxies that can be used to infer their mass distribution. Jeans modeling has been commonly used to estimate the mass distribution of dSphs (e.g Lokas, 2001; Kleyna et al., 2001; Battaglia et al., 2008b; Walker et al., 2007).

Jeans modeling is based on the assumption that a collisionless system is described by a distribution function (DF) $f(\mathbf{x}, \mathbf{v})$. The derivation of the Jeans equations from the continuity equation is shown in Appendix A. The Jeans equations are

$$0 = \frac{\partial \nu}{\partial t} + \frac{\partial(\nu \bar{v}_i)}{\partial x_i}, \quad (1.5)$$

$$\nu \frac{\partial \bar{v}_j}{\partial t} + \nu \bar{v}_i \frac{\partial \bar{v}_j}{\partial x_i} = -\nu \frac{\partial \Phi}{\partial x_j} - \frac{\partial(\nu \sigma_{ij}^2)}{\partial x_i}, \quad (1.6)$$

In the equation above, ν denotes the density, v_i is the i -th velocity moment, and $\sigma_{i,j}$ is the velocity dispersion tensor.

Binney & Tremaine (2008) describe a number of distribution functions for spherical and axisymmetric systems. While it is easy to calculate the velocity moments \mathbf{v} and $\overline{v_i v_j}$ given a DF, it is not straightforward to find a DF that is compatible with a given probability density distribution $\nu(\mathbf{x})$. Furthermore, not every solution to the Jeans equation corresponds to a physical DF. A DF is physical when it is non-negative everywhere. Depending on the galaxy that is modeled, it might be necessary to impose additional conditions that will lead to physical solutions. There exist techniques to infer moments from stellar densities without having to make prior assumptions about the DF. One of them is Schwarzschild modeling.

1.3.3 Schwarzschild modeling

Currently, Schwarzschild modeling is one of the favored techniques for determining the mass profiles of elliptical galaxies. It was developed by Schwarzschild (1979) and Richstone & Tremaine (1984). It is described as an orbit-based method since it combines orbits in order to match the light and kinematic distribution of a galaxy, which distinguishes it from particle-based N-body methods. Given a specific gravitational potential, a large number of orbits are integrated for many crossing times, in order to sample the entire phase space that is expected to be occupied by the galaxy. These form the orbit library and are weighted to obtain a model that fits the observed distribution. While the choice of the mass and light distributions might lead to unphysical DF in Jeans modeling, the DFs functions of the Schwarzschild method are always physical. However, due to the building and orbit-weighting processes, it is computationally more expensive and a smaller variety of gravitational potentials can be probed.

Despite its success on elliptical galaxies, the method has not been used that much on dSph galaxies. Jardel & Gebhardt (2012; 2013) model the Fornax and Draco dSphs using Schwarzschild modeling, and for Draco they find that the preferred model is a power-law with a NFW-like slope. The modeling work presented in this thesis is based on the Schwarzschild code of Maarten Breddels (Breddels et al., 2013), which he used to model the mass distributions of the Sculptor, Fornax, Carina, and Sextans dSphs (Breddels, 2013).

1.4 Outline of this thesis

The aim of this thesis is to apply Schwarzschild modeling to new observations of a large sample of individual stellar velocities in the Draco dSph galaxy. In Chapter 2 I describe new spectroscopic data of the Ursa Minor and Draco dSphs from AF2-WYFFOS at the William Herschel Telescope (WHT), La Palma. In Chapter 3 I describe the dynamical modeling of dwarf spheroidal galaxies using the Schwarzschild code developed by Breddels et al. (2013). In Chapter 4 I present the modeling results and in Chapter 5 I conclude.

Chapter 2

Data

In this chapter, I describe new optical spectroscopy of individual red giant branch (RGB) stars in the Ursa Minor and Draco dSphs. We observed several hundred stars using the AutoFib2 - Wide Field Fibre Optical Spectrograph (AF2-WYFFOS) at the William Herschel Telescope (WHT) during two observing runs in May 2014 and May 2015. The instrument was upgraded in 2012-2013, leading to a significant improvement of its performance. The AF2-WYFFOS combination consists of an automatic fiber positioner, which places the fibers within the one degree field of the prime focal plane. The 150 science fibers each have a diameter of 1.6 arcsec. Furthermore, for acquisition and guiding, up to 10 fiducial bundles can be used.

2.1 Observations

Targets for spectroscopic follow-up were selected from deep wide-field photometry from the MegaCam imager on the Canada France Hawaii Telescope. The photometric data of Draco have been published by Ségall et al. (2007) and of Ursa Minor by Muñoz et al. (2012). The selection regions on the galaxies' CMDs are shown in Figure 2.1.

The field of view of AF2-WYFFOS is one degree. However, fibers can only be placed within the inner radius of 25 arcmin, since optical distortions affect the fibers placed beyond that radius. The aim was to place the majority of science target fibers within the central 20 arcmin. Thus the galaxies were covered by 5 fields that overlapped slightly in order to have repeat measurements of some stars for calibration purposes. The field configurations were defined using the instrument's configuration software, which can be run automatically but requires some manual optimization. In each field, 70 - 90 fibers were placed on target stars. The remaining fibers were placed on blank patches of the sky to allow accurate sky subtraction on the science fibers. Each field was observed three times for 30 minutes and the resulting spectra were then combined.

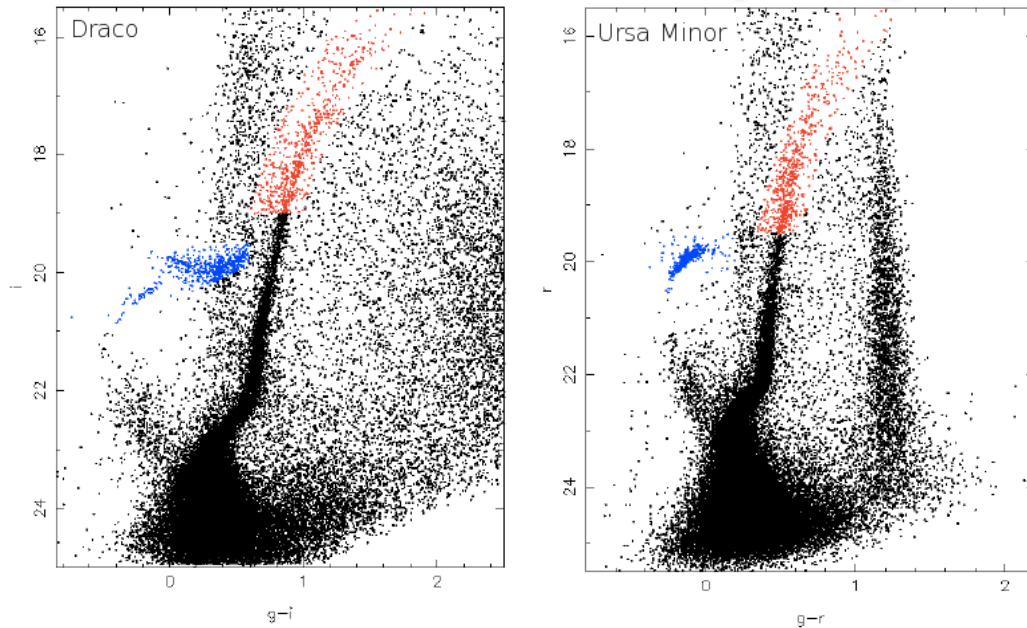


Figure 2.1: *CMDs of the Draco (left) and the Ursa Minor (right) dSphs within their tidal radius. The candidate RGB stars to be observed are shown in red and HB stars are shown in blue.*

2.2 Results

Since the data from our observing run in 2015 have not been reduced yet, we will only describe the results from observations on the nights of May 21-24 2014. After data reduction with a WEAVE¹ prototype pipeline at the Cambridge Astronomical Survey Unit by Mike Irwin and Jim Lewis, there are 400 line-of-sight velocities and metallicities ($[\text{Fe}/\text{H}]$) in Ursa Minor and 524 in Draco, which include some repeat measurements. The metallicities were determined using the CaII triplet (e.g Battaglia et al., 2008a; Starkenburg et al., 2010). In the following, we only consider spectra with a signal-to-noise ratio per Ångström (S/N per Å) greater than 12, which reduces the sample to 296 stars in Ursa Minor and 340 in Draco.

2.2.1 Velocity distribution and membership

In order to select likely member stars, we have a look at the distribution of stars in LOS-velocity-metallicity space, which is shown in Figure 2.2. Since the galaxies' systemic velocities are clearly distinct from the foreground stars' velocities, we can determine likely member stars based on their velocity. The foreground mainly consists of Milky Way halo and disk stars, which typically have heliocentric LOS velocities in the range of -200 to 100 km/s. Draco's systemic heliocentric LOS velocity is $v_{\text{Dra,sys}} = -293$ km/s and Ursa Minor's is $v_{\text{UMi,sys}} = -248$ km/s. Based on Figure 2.2, we choose to select stars within

¹WEAVE is a multi-object fiber spectrograph for the WHT, which is currently being built and expected to be operational by 2017.

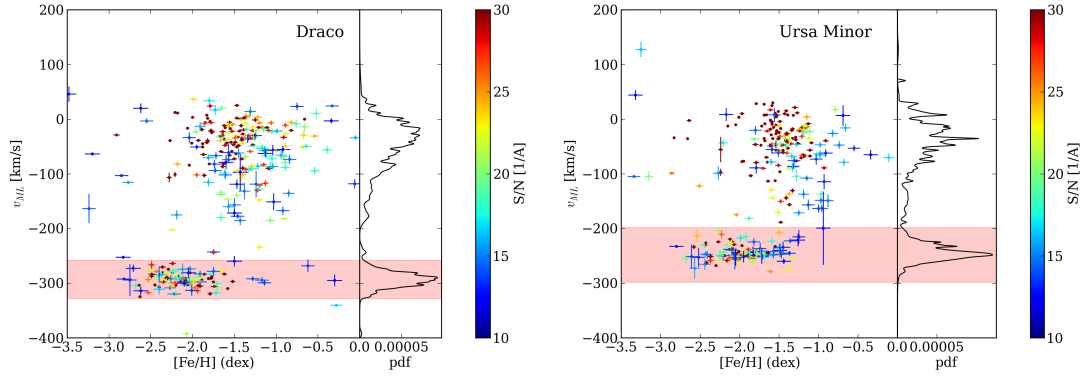


Figure 2.2: Metallicity versus heliocentric LOS velocity color coded by S/N per \AA of Draco (left) and Ursa Minor (right) and PDF of the LOS velocity. The membership regions are shaded in red and all stars outside this region are most likely non-members.

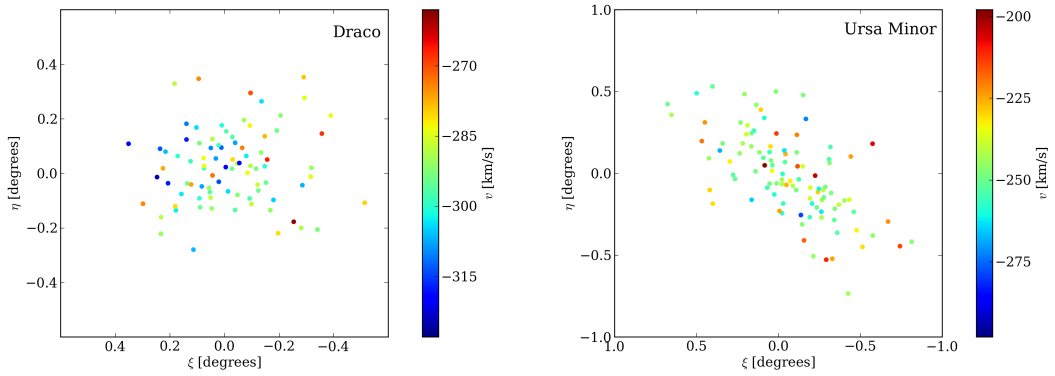


Figure 2.3: Spatial distribution of likely velocity member stars in Draco (left) and Ursa Minor (right) with S/N per \AA ≤ 12 . The stars are color-coded by their heliocentric LOS velocity.

approximately 3σ of the central velocity, which is $v = v_{\text{Dra,sys}} \pm 35$ km/s in Draco and with $v = v_{\text{UMi,sys}} \pm 50$ km/s in Ursa Minor. This leaves us with 99 likely member stars in Draco and 108 in Ursa Minor, which we will focus on in the following. The spatial distributions of likely member stars color-coded by their velocity are shown in Figure 2.3.

2.2.2 Metallicity distribution

The $[Fe/H]$ distribution is shown in Figures 2.4 and 2.5 for Draco and Ursa Minor. While there is no evidence for a metallicity gradient in Ursa Minor, there is a trend of decreasing metallicity towards the outskirts in Draco. We observe a large spread in metallicity in both galaxies. The lack of a metallicity gradient in Ursa Minor might be related to the dSph galaxy's tidal interaction with the MW that is also reflected in the dSph's morphology. Draco does not show any signs of tidal interaction with the MW. Its morphology has not been disturbed and therefore perhaps an intrinsic metallicity gradient has been preserved.

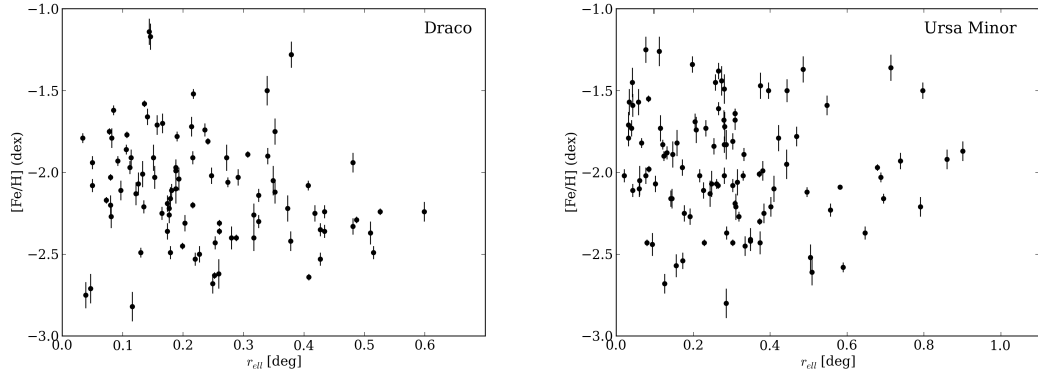


Figure 2.4: *Elliptical radius versus metallicity for the Draco (left) and Ursa Minor (right) dSphs.*

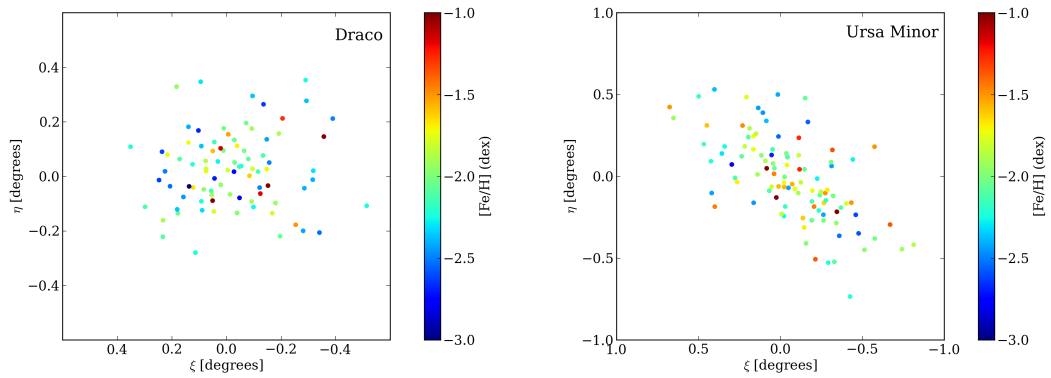


Figure 2.5: *Spatial distribution of likely velocity member stars in Draco (left) and Ursa Minor (right) with S/N per $\text{\AA} \leq 12$. The stars are color-coded by their metallicity.*

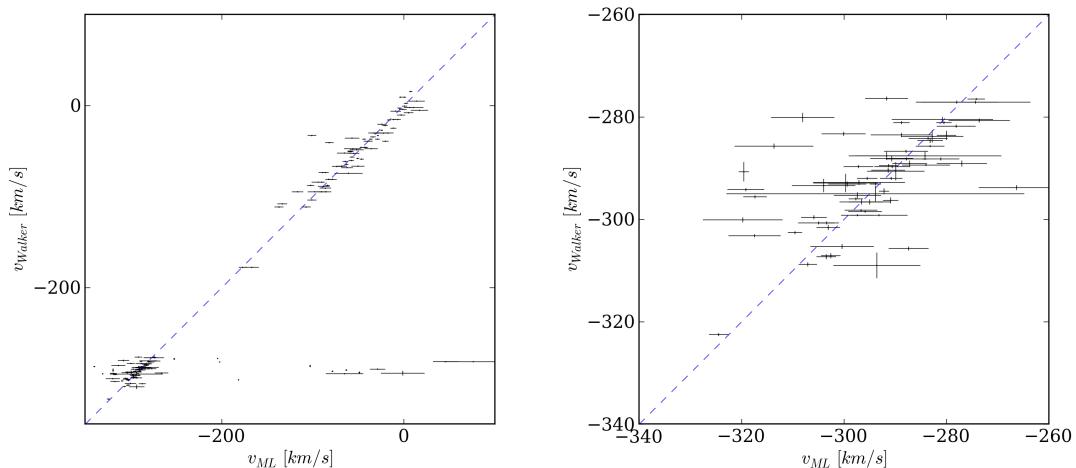


Figure 2.6: Comparison of the LOS velocities of stars present in our Draco data and published by WOM15. The right panel shows the likely velocity members.

2.3 Literature data

Another spectroscopic survey of Draco has recently been published by Walker, Olszewski & Mateo (2015; hereafter WOM15), which we can include in our Schwarzschild modeling. The authors observed more than 500 LOS velocity members with the 6.5 m-MMT/Hectochelle spectrograph. Their observed area is larger than the region we observed, and in the central region there are a number of stars that have also been observed by us. The largest radial distance from the center is 0.6 degrees in our observations, and in WOM15 observations it is 2 degrees, although there is some doubt about the membership beyond the tidal radius. Odenkirchen et al. (2001) determined Draco’s tidal radius to be at 0.7 degrees, however the definition of the tidal radius varies in the literature and different authors state different values ranging from 0.5 to 1 degree. We compare the LOS velocities and $[\text{Fe}/\text{H}]$ values for stars with $\text{S/N per } \text{\AA} \geq 12$ that overlap with WOM15’s catalog. WOM15 fit spectra using a Bayesian method.

Figure 2.6 shows the comparison of the LOS velocities. The velocities agree for most of the measurements for both likely Draco member stars and also for foreground stars. The origin of the clear discrepancy for some stars is currently unclear, but likely due to data reduction issues in our data.

WOM15 determined $[\text{Fe}/\text{H}]$ using the Mg b triplet and FeII lines. As shown in Figure 2.7, there is a scatter in the comparison between our $[\text{Fe}/\text{H}]$ values and those of WOM15. The investigation of this scatter lies beyond the scope of this thesis, since we will use only their velocity measurements.

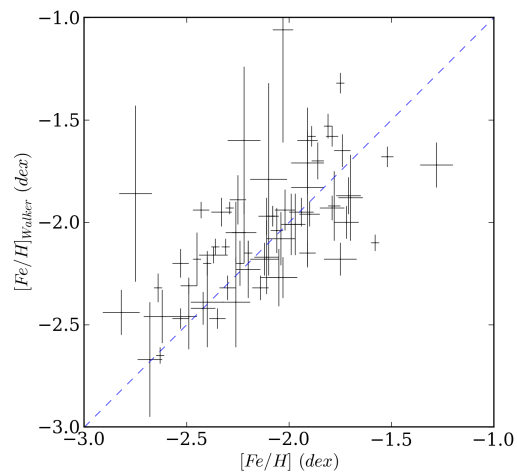


Figure 2.7: Comparison of the $[Fe/H]$ values of likely velocity member stars present in our Draco data and published by WOM15.

Chapter 3

Schwarzschild modeling

In this chapter, I introduce the Schwarzschild method that we use to model our data. It was developed by Schwarzschild (1979) to determine the numerical model of a triaxial system in dynamical equilibrium. With the rapid increase of spectroscopic datasets in recent years, it has become more popular to model the kinematic properties of dSphs using this method. In this thesis, I use the Schwarzschild code developed by Breddels (2013) and Breddels et al. (2013), which is based on the ideas of Rix et al. (1997) and van den Bosch et al. (2008), and has been optimized for spherical symmetry. It has been used to model the Fornax, Sculptor, Carina, and Sextans dSphs. Below, I first explain the general modeling procedure and then explore the method using a Sculptor-like mock galaxy.

3.1 The method

In the following, I will explain the three main steps of the Schwarzschild method. In general, they can be summarized as follows (e.g., Rix et al., 1997):

1. A representative library of orbits is calculated in a given potential.
2. The orbits are projected onto the space of observables.
3. The combination of orbits with (non-negative) weights that fits the observed data best is determined.

The DF can be inferred from the orbit weights, which are determined in the last step. By construction, the orbit weights and the resulting DF are always non-negative. This is in contrast to Jeans modeling, where, without additional constraints, the DF corresponding to a solution of the Jeans equations can be negative. In Schwarzschild modeling, no assumptions about the form of the distribution function are made. Even though we restrict ourselves to a spherically symmetric model, the Schwarzschild method can be used to model many different geometries and functional forms of potentials and the model can have different components. The model we use consists of a simple stellar component embedded in a DM halo.

In the remainder of this chapter, I will describe the Schwarzschild method developed by Maarten Breddels. A detailed description can be found in Breddels (2013).

3.1.1 Density distribution and model parameters

We can describe the dSphs using a Plummer profile embedded in a DM halo. Both components are spherically symmetric. Since we can assume that the light distribution is accurately known from observations, the parameters of the stellar component are fixed, while we vary the set of parameters describing the DM halo.

Stellar component

The Plummer potential was introduced by Plummer (1911) in order to describe globular clusters. Its functional form is

$$\Phi_{\text{Plummer}}(r) = -\frac{GM}{\sqrt{r^2 + b^2}}, \quad (3.1)$$

where M is the system's total mass and b the Plummer scale length, which sets the linear scale of the model. The corresponding density can be derived using Poisson's equation and is

$$\rho_{\text{Plummer}}(r) = \frac{3M}{4\pi b^3} \left(1 + \frac{r^2}{b^2}\right)^{-5/2}. \quad (3.2)$$

Dark matter halo

For the DM halo, I compared two density distributions. The first one is a **NFW profile** (Navarro, Frenk & White, 1996), which is a well-known and well-used profile for fitting the density distribution of DM halos in cosmological N-body simulations. The density distribution is defined as

$$\rho_{\text{NFW}}(r) = \frac{\rho_0}{(r/r_s)(1 + r/r_s)^2}. \quad (3.3)$$

It is governed by the density parameter ρ_0 and the scale radius r_s . The density parameter is related to the NFW halo concentration c :

$$\frac{\rho_0}{\rho_{\text{crit}}} = \frac{200}{3} \frac{c^3}{\ln(1+c) - c/(1+c)}, \quad (3.4)$$

where $\rho_{\text{crit}} = 3H^2/8\pi G$ is the critical density in a Λ CDM Universe.

The potential corresponding to the density in equation (3.3) is

$$\Phi_{\text{NFW}}(r) = -4\pi G \rho_0 r_s^2 \frac{\ln(1 + r/r_s)}{r/r_s}, \quad (3.5)$$

which can be derived using Poisson's equation.

The second profile is a modified Dehnen profile (Dehnen, 1993), which we simply call the **cored profile**. It follows the density distribution

$$\rho_{\text{core}}(r) = \frac{\rho_0}{(1 + (r/r_s)^\gamma)^{\beta/\gamma}}, \quad (3.6)$$

which also has the free parameters r_s and ρ_0 . It is further described by the outer slope, β , and the parameter γ , which quantifies the transition between the inner and the outer slope of the profile. The corresponding potential is calculated numerically, since no analytic expression exists for this profile. Poisson's equation is solved numerically using a Finite Element Method. This has been tested in the case of the NFW profile and it has been found that the relative errors are of the order of 10^{-6} (Breddels et al., 2013).

Model parameters

Both potentials are governed by the parameters r_s and ρ_0 . The cored model has two further parameters β and γ . Following Breddels & Helmi (2013), we choose $\beta = 3$ and $\gamma = 1$ and keep these parameters fixed. First we model the mass enclosed within 1 kpc, $M_{1 \text{ kpc}}$, and the scale radius, r_s . In order to express the potential using these two parameters, the enclosed mass at radius r can be calculated using

$$M_{\text{encl}}(r) = \int_0^r 4\pi r'^2 \rho(r') dr' \quad (3.7)$$

and can then be related to the density parameter ρ_0 . The mass profiles for the two DM profiles described in the previous section are thus:

$$M_{\text{NFW}}(r) = 4\pi\rho_0 r_s^3 \left(\ln(1 + r/r_s) - \frac{r/r_s}{1 + r/r_s} \right) \quad (3.8)$$

$$M_{\text{core}}(r) = 4\pi\rho_0 r_s^3 \left(\ln(1 + r/r_s) - \frac{r(3r + 2r_s)}{2(r + r_s)^2} \right) \quad (3.9)$$

Breddels & Helmi (2013) studied the shape of the mass distribution in different DM halo profiles including the cored and the NFW profiles for the dSph galaxies Fornax, Sculptor, Carina, and Sextans. They find that there is a radius at which all the best-fit DM density profiles have a similar logarithmic slope, $\kappa = d \log \rho / d \log r$. While the logarithmic slope is similar, the linear slope $d\rho/dr$ can be quite different. This radius is near the position where the logarithmic slope of the stellar density profile is -3 . It is denoted by r_{-3} . For a Plummer profile, the logarithmic slope is

$$\kappa = \frac{d \ln \rho_{\text{Plummer}}}{d \ln r} = -\frac{5r^2}{b^2 + r^2} \quad (3.10)$$

and the radius at which it is -3 is

$$r_{-3} = \sqrt{\frac{3}{2}}b. \quad (3.11)$$

The finding that there is a finite region where the mass determination is more accurate has also been made by other authors using Jeans modeling (Wolf et al., 2010; Walker, 2013; Jardel et al., 2013). Therefore, another pair of free parameters is introduced, which are recovered at r_{-3} , being the enclosed mass M_{-3} , and the corresponding logarithmic slope of the DM density profile, $\kappa(r_{-3}) = \kappa_{-3}$. For the two profiles described in the previous section, we derive

$$\kappa(r) = \frac{d \ln \rho}{d \ln r} \quad (3.12)$$

and find the following relations between κ_{-3} and r_s :

$$r_{s,\text{NFW}} = -r \frac{\kappa + 3}{\kappa + 1} \quad (3.13)$$

$$r_{s,\text{core}} = r \left(\frac{-\kappa}{\beta + \kappa} \right)^{-1/\gamma} \quad (3.14)$$

3.1.2 Orbit integration

In the first step, 10240 orbits are integrated in the potentials described above. The number of orbits integrated is related to the observables, as is explained in the following section. The equations of motions are integrated using the GNU scientific library ODE solver (8th order Runge-Kutta Dormand-Prince method). The total energy is conserved up to $\pm 0.1\%$. The orbital timescale is

$$t_{\text{orb}} = \frac{2\pi r_a}{v_{\text{circ}}}, \quad (3.15)$$

where r_a is the orbit's apocentre radius and v_{circ} the circular velocity at that radius. The orbits are integrated for 100 orbital timescales and stored at 1000 points, which results in a (constant) step size of $0.1 t_{\text{orb}}$. Since the system is spherically symmetric, the orbits are integrated in a two-dimensional plane. In order to obtain a three-dimensional orbit library, each orbit is subsequently randomly rotated 25 times after a complete orbit has been computed.

3.1.3 Observables

Having calculated the orbit library, in the second step, the orbits are projected onto the space of observables. From the observations, the light distribution and the moments of the LOSVD can be inferred. The system is governed by a DF, which we want to recover. In contrast to other modeling techniques, as for example Jeans modeling, Schwarzschild modeling does not assume that the DF has a certain functional form, but that it is a sum of Dirac δ -functions on a grid in energy (E) and angular momentum (L) space:

$$f(E, L) = \sum_{i,j} \hat{f}_{i,j} \delta(E - E_i) \delta(L - l_j L_{\text{max},i}) \quad (3.16)$$

To obtain a rectangular grid, the relative angular momentum $l = L/L_{\max}$ is used.

In order to calculate the orbit weights, the orbits are compared with the observables. In principle, this would mean that the number of free parameters that define the DF equals the number of orbits. Instead of determining the orbit weights for every orbit separately, we determine them for small volumes in phase space by adding neighboring orbits. The volume consists of $N_{d_E} \times N_{d_l} = 8 \times 8 = 64$ orbits, which share the same DF coefficient. This concept is also known under the name of dithering. Thus the DF is described by $N_E \times N_l = (N'_E \times N'_l)/(N_{d_E} \times N_{d_l})$ free parameters. For $N_E = 20$ and $N_l = 8$, the distribution function has 160 free parameters. In total we integrate 10240 orbits.

The 6D-phase-space information contained in the orbit library needs to be translated into observables. We distinguish between observables derived from the light distribution and observables derived from the LOSVD.

Light distribution

First the light distribution in 250 projected radial bins is calculated. Under the assumption that mass equals light for the stellar component, the mass contributed by the orbits in each bin is determined. First, the normalized mass is introduced as

$$\frac{dm_{\star}(R)}{M_{\star}} = 2\pi R \Sigma_0(R) dR, \quad (3.17)$$

where Σ_0 is the surface brightness per area of the galaxy. The mass contributed by the orbit i, j with energy E_i and relative angular momentum l_j in bin k is

$$\frac{\Delta m_{\star, i, j, k}}{M_{\star}} = \int_{R_k}^{R_{k+1}} 2\pi R \Sigma_{0, i, j}(R) dR \quad (3.18)$$

This is equal to the fractional time the orbit has spent in bin k . This can be determined by counting the number of times the orbit crosses the bin and dividing it by the total number of time steps, since the time step is fixed. The total mass contributed by all orbits in bin k is thus

$$\frac{\Delta m_{\star, k}}{M_{\star}} = \sum_{i=1}^{N'_E} \sum_{j=1}^{N'_l} \underbrace{g(E_i, L_j) \hat{f}_{i, j} L_{\max} \Delta E_i \Delta l_j}_{c'_{i, j}} \times \frac{\Delta m_{\star, i, j, k}}{M_{\star}} \quad (3.19)$$

where $g(E, L)$ is the density of states and $c'_{i,j}$ the orbital weights that have to be determined. Having determined the light profile $\Sigma_\star(R)$ from photometric observations, one can calculate the projected mass in each bin:

$$\frac{\Delta m_{\star, \text{true}, k}}{M_\star} = \int_{R_k}^{R_{k+1}} 2\pi R \Sigma_\star(R) dR \quad (3.20)$$

The difference in projected mass between the model and the observations is required to be smaller than one percent:

$$\left| \frac{\Delta m_{\star, \text{true}, k}}{M_\star} - \frac{\Delta m_{\star, k}}{M_\star} \right| \leq 0.01 \quad (3.21)$$

Kinematics

After having derived the expressions for the observables from the light distribution, a similar procedure is used to determine the moments of the LOSVD. The projected second and fourth moments of the LOSVD in bin k are

$$\mu_{2,k} = \frac{M_\star}{\Delta m_{\star, k}} \sum_{i=1}^{N'_E} \sum_{j=1}^{N'_l} c'_{i,j} \int_{R_k}^{R_{k+1}} 2\pi R \mu_{0,i,j}(R) \mu_{2,i,j}(R) dR \quad (3.22)$$

$$\mu_{4,k} = \frac{M_\star}{\Delta m_{\star, k}} \sum_{i=1}^{N'_E} \sum_{j=1}^{N'_l} c'_{i,j} \int_{R_k}^{R_{k+1}} 2\pi R \mu_{0,i,j}(R) \mu_{4,i,j}(R) dR, \quad (3.23)$$

where $\mu_{0,i,j}(R)$, $\mu_{2,i,j}(R)$, and $\mu_{4,i,j}(R)$ are the zeroth, second, and fourth moments of orbit i, j . Similar to determining the projected mass in each bin, to evaluate the integrals in the equations above, the number of times an orbit crosses bin k is counted. For every count, the sum of the second (fourth) moment of the LOSVD in quadrature (to the fourth power) is added. The final sum is divided by the number of time steps.

The n -th moment of the LOSVD is

$$\text{Exp}[m_n] = \text{Exp} \left[\frac{1}{N} \sum_i^N (v_i + \epsilon_i)^n \right], \quad (3.24)$$

where v_i is the i -th velocity measurement and ϵ_i is the associated unknown measurement noise, which is assumed to be drawn from a normal distribution. The average of the estimated squared errors is

$$s_2 = \text{Exp} \left[\frac{1}{N} \sum_i^N \epsilon_i^2 \right]. \quad (3.25)$$

Hence the estimator of the second moment is

$$\hat{\mu}_2 = \frac{1}{N} \sum_i^N (v_i + \epsilon_i)^2 - s_2. \quad (3.26)$$

Along the same lines, the estimator of the fourth moment is found to be

$$\hat{\mu}_4 = \frac{1}{N} \sum_i^N (v_i + \epsilon_i)^4 - 3s_2^2 - 6\mu_2 s_2. \quad (3.27)$$

The variance of the variable x is defined as $\text{var}(x) = \text{Exp}[x^2] - (\text{Exp}[x])^2$. The variances of the estimators are

$$\text{var}(m_2) = \frac{1}{N} (\mu_4 - \mu_2^2 + 2s_2^2 + 4\mu_2 s_2) \quad (3.28)$$

$$\text{var}(m_4) = \frac{1}{N} (\mu_8 + 105s_2^4 + 204\mu_4 s_2^2 + 420\mu_2 s_2^3 + 28\mu_6 s_2 - 9s_2^4), \quad (3.29)$$

where μ_6 and μ_8 are the sixth and eighth moment of the LOSVD. The variances of the moments are needed in the following step, where a solution is found using χ^2 -fitting.

3.1.4 Finding a solution

In order to find a solution, the likelihood of the kinematic data given a model is calculated. The likelihood is

$$p(\text{kinematic data}|\text{model}) \propto \exp\left(\frac{1}{2}\chi_{\text{kin}}^2\right) \quad (3.30)$$

with

$$\chi_{\text{kin}}^2 = \sum_k^{N^{\text{bin}}} \frac{(\hat{\mu}_{2,k} - \mu_{2,k})^2}{\text{var}(\hat{\mu}_{2,k})} + \sum_k^{N^{\text{bin}}} \frac{(\hat{\mu}_{4,k} - \mu_{4,k})^2}{\text{var}(\hat{\mu}_{4,k})}. \quad (3.31)$$

The moments $\mu_{2,k}$ and $\mu_{4,k}$ are calculated from the orbits via equations (3.22) and (3.23) under the assumption that $\text{var}(m_n) \approx \text{var}(\hat{\mu}_n)$. The estimators $\hat{\mu}_{2,k}$ and $\hat{\mu}_{4,k}$ are determined from the observed LOSVD profile. Quadratic programming (QP) is used to find the coefficients $c_{i,j}$ that maximize the likelihood p and fulfill the requirements that $c_{i,j} \geq 0$ and $\sum_i \sum_j c_{i,j} = 1$. QP is a numerical method that is used to solve a quadratic optimization problem with linear constraints.

Even though the parameter space has already been significantly reduced using dithering, it is still rather large, which can lead to spiky DFs. Therefore, a regularization constraint is introduced (Cretton et al., 1999; van den Bosch et al., 2008), which effectively reduces the parameter space further. It is added as a penalty term

$$\chi^2 = \chi_{\text{kin}}^2 + \chi_{\text{reg}}^2 \quad (3.32)$$

Since the regularization term is also quadratic, QP can still be used to minimize equation (3.32). We use the same regularization constraint as Breddels et al. (2013). The problem

is defined by the linear constraints on the light distribution (equation (3.21)) and the constraints on the DF coefficients $c_{i,j}$.

3.2 Testing the method using a Sculptor-like mock galaxy

In order to (re-)test the method, we use a Sculptor-like mock galaxy, which has been created according to previously published dynamical models of the system (Battaglia et al., 2008b) by Breddels et al. (2013). The stellar component is a Plummer sphere with stellar mass $M_\star = 10^6 M_\odot$ and scale radius $b = 0.3$. It is embedded within a spherical NFW DM halo with scale radius $r_s = 0.5$ kpc and mass $M_{1\text{kpc}} = 10^8 M_\odot$ enclosed within 1 kpc. We model two data sets, one with 2000 stars randomly chosen from the mock galaxy and one with 200 randomly chosen stars, since this is approximately the size of the data set we obtained for Draco.

As shown in panel (a) of Figure 3.1, we correctly recover the NFW input parameters, however, with only 200 stars, both the scale radius and the logarithmic slope are very unconstrained. In the following plots, the relative likelihood of the model is shown, which is $p_{\text{rel}} = p / \max(p)$. Besides being of interest for studying the effect of different sample sizes, these tests are also useful to evaluate whether the same scale radius is recovered when using the slope κ_{-3} as a free parameter instead. Using equations (3.13) and (3.14), we convert the recovered slopes to the corresponding halo scale radii and find $r_{s,\text{NFW}} = 0.86$ kpc and $r_{s,\text{core}} = 0.27$ kpc. Recalling that the true halo scale radius is 0.5 kpc, we find that the recovered NFW scale radius is a nearly factor of two too large. We do not recover the true value, however it lies within the 2σ contours. For the sample of 2000 stars, the best-fit slopes of the cored and the NFW profile are both $\kappa \approx -1.6$. Cored profiles always have a smaller scale radius, if we require that the slopes are the same at r_{-3} for the cored and the NFW profiles, since

$$\frac{r_{s,\text{NFW}}}{r_{s,\text{core}}} = \frac{\kappa}{\kappa + 1}. \quad (3.33)$$

It is therefore not surprising that we recover a smaller scale radius using the cored model.

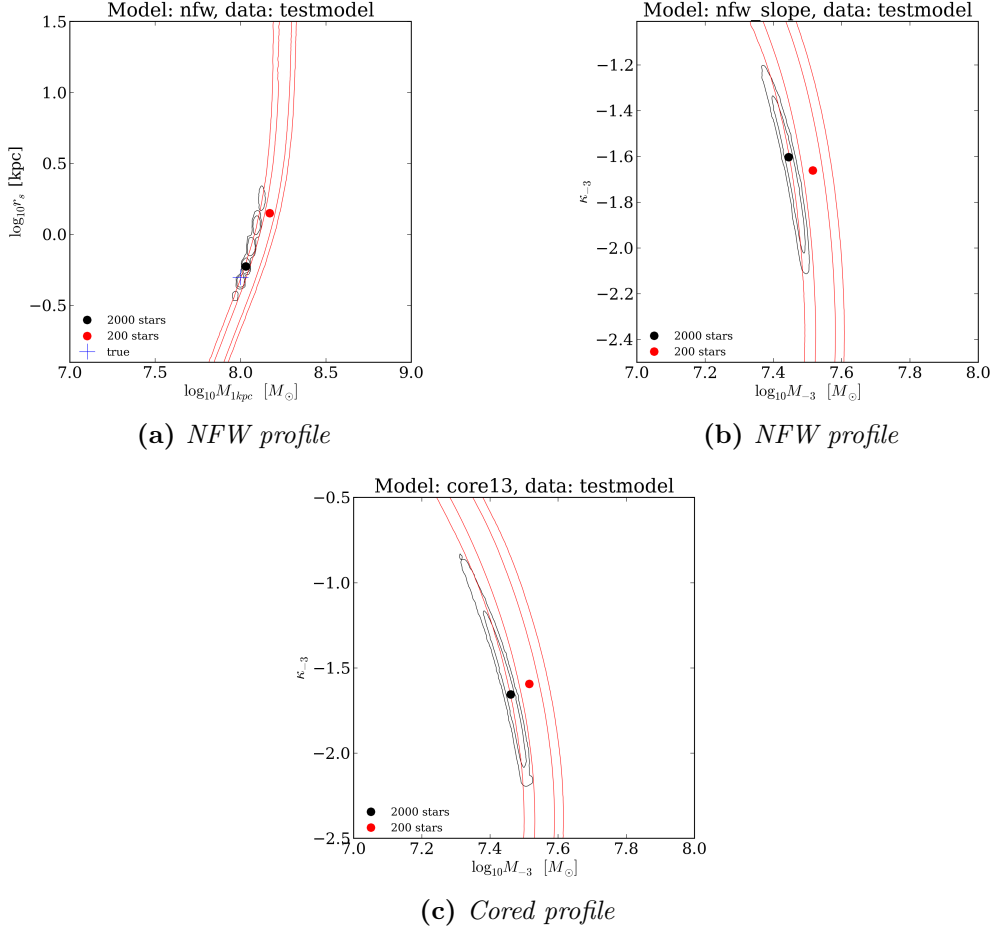


Figure 3.1: Relative likelihood contours for the two parameters κ_{-3} and M_{-3} characterizing the NFW profile (a, b) and the cored profile (c) for a Sculptor-like mock galaxy. The free parameters in (a) are the $M_{1\text{kpc}}$ and r_s and in (b) and (c) they are M_{-3} and κ_{-3} . Shown in black and red are the 1- and 2 σ contours for datasets consisting of 2000 and 200 stars respectively, using equidistant binning. The highest likelihood is denoted by a dot in the respective color.

Chapter 4

Schwarzschild modeling of the Draco dSph galaxy

In the previous chapter I explained the Schwarzschild method and tested it with the help of a Sculptor-like mock dSph galaxy. In the following I present the results from modeling the Draco dSph using the spectroscopic data presented in Chapter 2, including observations from WOM15.

4.1 Setting up the modeling

4.1.1 Model parameters

The stellar component of the model is a Plummer sphere governed by the observed properties of Draco, namely the stellar mass $M_\star = 2.6 \times 10^5 M_\odot$ (Mateo, 1998) and the scale length $b = 0.24$ kpc (Ségall et al., 2007). The ellipticity is 0.29 and the corresponding position angle 82.1° (Mateo, 1998). As described in the previous section, we model two different dark matter halos, a cored profile and a NFW profile. For the latter, we explore two sets of free parameters: the scale radius r_s and the DM mass enclosed at 1 kpc, $M_{1\text{kpc}}$, and the logarithmic slope κ_{-3} and the mass M_{-3} , both evaluated at radius r_{-3} . For a Plummer profile governed by the given parameters, this radius can be calculated using equation (3.11) and is at 0.30 kpc.

In the following figures and tables, we denote our dataset with WHT and the data from WOM15 by the author abbreviation. We introduce the following nomenclature for the models:

- **nfw** NFW profile with free parameters r_s and $M_{1\text{kpc}}$
- **nfw_slope** NFW profile with free parameters κ_{-3} and M_{-3}
- **core13** Cored profile with free parameters κ_{-3} and M_{-3} and fixed parameters $\beta = 3$ and $\gamma = 1$

4.1.2 Binning

Breddels et al. (2013) suggest that at least 250 stars per bin are required to obtain accurate estimates of the fourth moment of the LOSVD. Given the limited size of our dataset, we restrict ourselves to only determining the likelihood from the second moment, which requires about 50 stars per bin. Our own observations consist of 99 velocity members and we obtain additional 560 from WOM15. We compare different binning techniques. We bin the data into

1. equidistant bins,
2. bins covering the same area,
3. and bins containing the same number of stars.

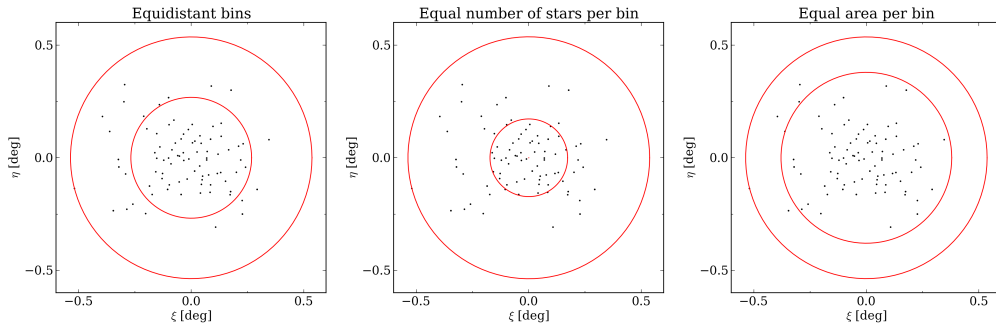


Figure 4.1: *Spatial distribution of stars in Draco observed by us (WHT)* Shown in red are the two radial bins for (from left to right) equidistant binning, bins containing the same number of stars, and bins covering the same area.

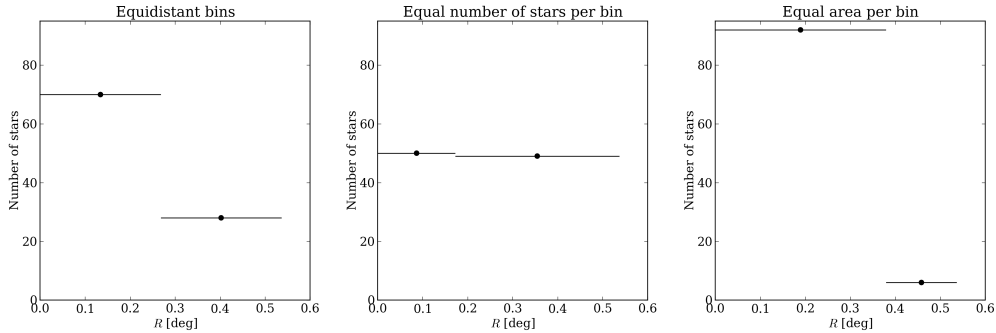


Figure 4.2: *Histograms of the star counts of the bins presented in Figure 4.1.* Shown from left to right are the two radial bins for equidistant binning, bins containing the same number of stars, and bins covering the same area.

The three different binnings for the WHT data are shown in Figure 4.1 and the corresponding star counts per bin are shown in Figure 4.2. The number of stars allows no more than two bins, which is in fact the minimal number of bins required by the modeling. From the star-count histograms, it can be seen that the results from equidistant and equal-area

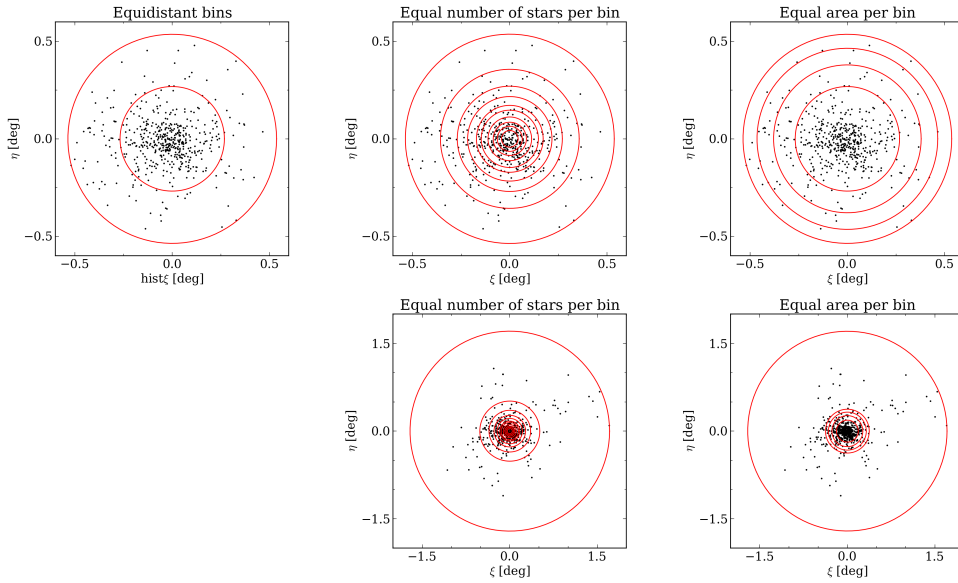


Figure 4.3: *Spatial distribution of stars in Draco observed by WOM15. The top row shows the bins which cover the data in the same radial range as ours and the bottom row the full data range. Shown from left to right are the two radial bins for equidistant binning, bins containing the same number of stars, and bins covering the same area.*

binning have to be interpreted with caution, since number of stars in the outer bins is significantly smaller than 50.

Since the WOM15 data contains roughly five times more stars, we can use a larger number of bins. In order to better compare the results from modeling our own observations to those obtained from modeling the data of WOM15, we also model only the stars which fall into the bins we use for modeling our own data. Since there is some doubt about the membership of stars beyond the tidal radius, regardless of the binning, the outer bin always consists of the stars beyond the tidal radius. This is shown in Figure 4.3. Figure 4.4 shows histograms of the number of stars contained in each bin for the different datasets. When using equidistant bins or bins which cover the same area, there are significantly fewer stars in the outer bins compared to the inner ones. Again, this needs to be kept in mind when analyzing the resulting LOSVD profiles for the binned data and the corresponding modeling results.

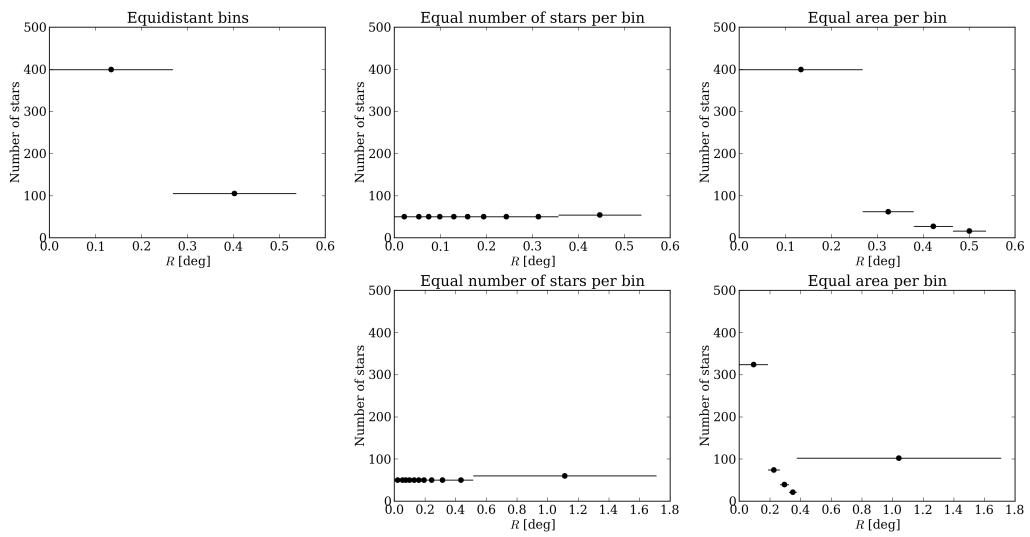


Figure 4.4: Histograms of the radius versus the number of stars in each bin. From top left to bottom right: Our data with equidistant bins, WOM15 data in the same radial range and the same bins, WOM15's data in the same radial range with bins containing ~ 50 stars, and Walker's data in the full radial range with bins containing ~ 50 stars.

4.2 Results

We model the two datasets independently. Since the origin of the clear discrepancy between the velocity measurements of a number of stars is still unclear, but likely due to data reduction issues in our data (cf. Section 2.3), we refrain from modeling the combined dataset until our data has been reprocessed. In the following section, I present and compare the results from modeling the WHT and WOM15 datasets.

4.2.1 WHT data

We use the three different binning techniques described in Section 4.1.2 to model the WHT data. Figure 4.5 shows the likelihood contours and best-fit parameter values of the DM halo profiles obtained using Schwarzschild modeling. The best-fit values are presented in Table 4.1. Using equations (3.13) and (3.14), we can relate the logarithmic slopes κ_{-3} to the respective scale radii of the profiles, which are also stated in Table 4.1. The elongated contours in Figure 4.5 indicate that the DM halo’s scale radius is much less constrained than the halo mass for both the NFW and the cored profile. The shape and extend of the likelihood contours is similar to the ones obtained for a Sculptor-like test galaxy using a random sample of 200 stars (Figure 3.1).

We obtain the velocity dispersion profiles from modeling the second moment of the LOSVD. Figure 4.6 shows the LOS velocity dispersion profiles corresponding to the best-fit values along with the velocity dispersion profiles of the binned data for the different DM halo profiles and binning techniques. The binned velocity dispersion profiles are flat within the errors. The modeled velocity dispersion profiles agree well with the observed ones and there are no qualitative differences between the modeled velocity dispersion profiles of different DM halos.

It is apparent from Figure 4.5 and Table 4.1 that the best-fit parameters of both the NFW and the cored profile are quite similar when using equidistant bins or bins containing an equal number of stars (blue and black dots), while a much lower slope κ_{-3} and scale radius r_s are recovered when using bins covering the same area (red dots). The 1σ confidence contours overlap, however, the overlapping region does not enclose the best-fit parameter values.

This discrepancy can be explained looking at the binned LOS velocity dispersion profiles in Figure 4.6. The modeling results in a decreasing velocity dispersion when using bins covering the same area. However, we do not attribute this decrease to physical properties of the dSph, but rather due to the fact that the outer bin only contains 10 stars. Recalling that 50 stars per bin are recommended, this result should be interpreted with caution. Nonetheless, it indicates that a small change in the velocity dispersion profile results in a shift in the recovered logslope or scale radius, while the mass is not affected strongly. Ultimately, we expect that the “true” values lie in the regions in which the contours overlap.

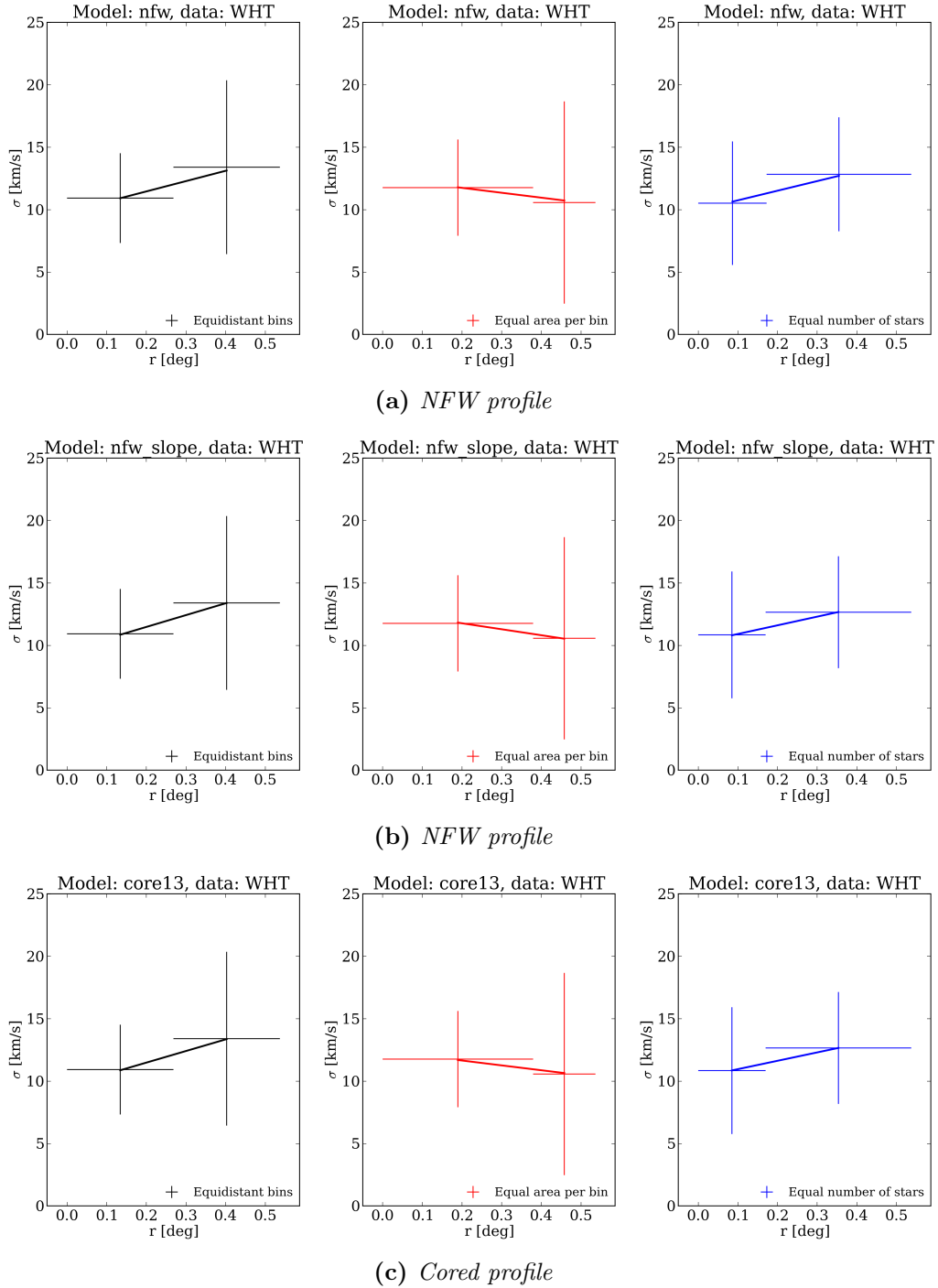


Figure 4.6: Modeled LOS velocity dispersion profiles NFW profile (a, b) and the cored profile (c) for WHT data. The colors correspond to the color scheme in Figure 4.5. The errorbars are the binned velocity dispersion profiles obtained from the data. The width of the error bar indicates the radial bin width.

Model	nfw		nfw_slope			core13		
Parameters	$M_{1\text{kpc}}$	r_s	M_{-3}	κ_{-3}	r_s	M_{-3}	κ_{-3}	r_s
Data	[M_\odot]	[kpc]	[M_\odot]		[kpc]	[M_\odot]		[kpc]
WHT (1)	2.05×10^8	13.3	2.21×10^7	-1.10	5.89	2.33×10^7	-1.13	0.491
WHT (2)	2.37×10^8	0.365	2.27×10^7	-1.07	7.82	2.46×10^7	-1.17	0.460
WHT (3)	1.15×10^8	3.35	2.89×10^7	-1.96	0.32	2.89×10^7	-1.97	0.155

Table 4.1: Best-fit results for the free parameters of the NFW and cored profiles. The left column indicates which dataset was used. The number in brackets behind WHT corresponds to the binning routine used (cf. Section 4.1.2).

Model	nfw		nfw_slope			core13		
Parameters	$M_{1\text{kpc}}$	r_s	M_{-3}	κ_{-3}	r_s	M_{-3}	κ_{-3}	r_s
Data	[M_\odot]	[kpc]	[M_\odot]		[kpc]	[M_\odot]		[kpc]
WOM15 (1)	1.65×10^8	31.6	1.68×10^7	-1.05	11.5	1.55×10^7	-0.797	0.815
WOM15 (2)	1.71×10^8	31.6	1.55×10^7	-1.05	11.5	1.39×10^7	-0.719	0.936
WOM15 (3)	1.65×10^8	31.6	1.51×10^7	-1.05	11.5	1.29×10^7	-0.609	1.16
WOM15 (2)	1.65×10^8	31.6	1.55×10^7	-1.05	11.5	1.21×10^7	-0.516	1.42
WOM15 (3)	1.65×10^8	31.6	1.55×10^7	-1.05	11.5	1.25×10^7	-0.562	1.27

Table 4.2: Best-fit results for the free parameters of the NFW and cored profiles. The left column indicates which dataset was used. The number in brackets behind WOM15 corresponds to the binning routine used (cf. Section 4.1.2). The results in the top half of the table were obtained using data within a radius of 0.6 degrees and the results in the bottom half using the full dataset.

The velocity dispersion profiles obtained from modeling the second moment of the LOSVD are shown in Figure 4.8. The observed velocity dispersion profiles all show a slight increase of velocity dispersion with increasing radius for all three binning techniques. A similar trend has been observed by Walker et al. (2009) based on MMT/Hectochelle data extending out to 0.55 degrees. The modeled dispersion profiles follow the same trend for all DM halo profiles.

We then model the full dataset. As we already explained in Section 4.1.2, the outermost bin consists of stars beyond a radius of 0.6 deg. Figure 4.9 shows the likelihood contours and best-fit parameter values for the different DM profiles. The corresponding best-fit values are presented in the bottom half of Table 4.2. The inclusion of data beyond a radius of 0.6 degrees results in much smaller and less elongated confidence contours, while the recovered best-fit parameters are similar. Figure 4.10 shows a further increase of the velocity dispersion in the outermost bin. Since there is still some doubt about the membership of stars beyond the tidal radius, this might not be due to an intrinsic cause, but to contamination of the data by non-member stars.

4.2.3 Comparison

I presented the results from individually modelling the WHT and WOM15 datasets in the previous two sections. Figure 4.11 facilitates the comparison of the results, showing the likelihood contours of the recovered parameters using the same equidistant bins. For

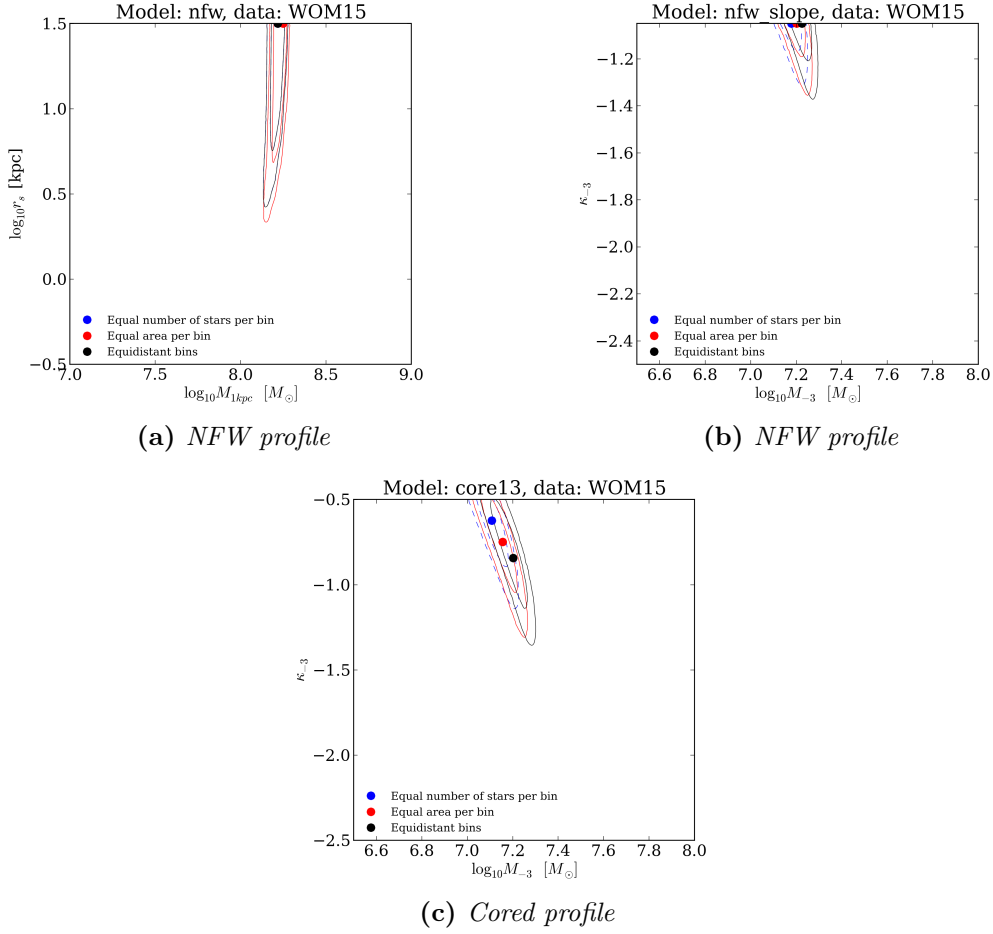


Figure 4.7: Relative likelihood contours for the two parameters κ_{-3} and M_{-3} characterizing the NFW profile (a, b) and the cored profile (c) for WOM15 data within a radius of 0.6 degrees. Shown in black (red, blue) are the 1- and 2σ contours for data using equidistant bins (an equal area per bin, an equal number of stars per bin). The highest likelihood is denoted by a dot in the respective color.

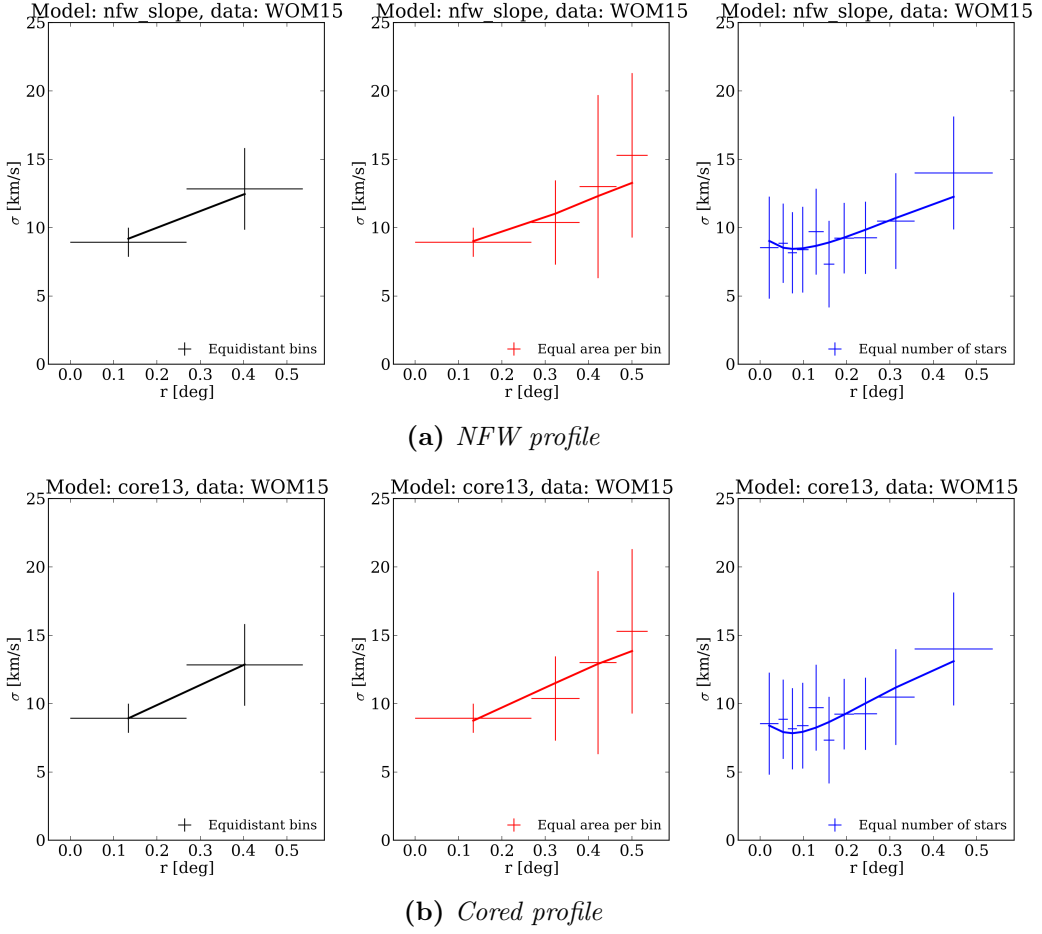


Figure 4.8: Modeled LOS velocity dispersion profiles NFW profile (a) and the cored profile (b) for WOM15 data within a radius of 0.6 degrees. The colors correspond to the color scheme in Figure 4.7, shown in black (red, blue) are the profiles and data calculated using equidistant bins (an equal area per bin, an equal number of stars per bin).

all models and parameters chosen, the 2σ -confidence contours overlap. As expected from a larger dataset, the contours on the best-fit values modeled using WOM15 data are smaller. As we have already explained in the previous two sections, a mere comparison of the best-fit parameters, especially for the scale radius, is difficult due to the large likelihood contours. However, the DM halo mass at r_{-3} is better constrained. Using the WHT data, we recover a mass of $2.21 \times 10^7 M_{\odot}$ for the NFW profile and a mass of $2.33 \times 10^7 M_{\odot}$ for the cored profile, while the NFW halo mass is $1.68 \times 10^7 M_{\odot}$ and the cored halo mass is $1.55 \times 10^7 M_{\odot}$, using the same equidistant bins both time. Comparing Tables 4.1 and 4.2, we find that the recovered mass is always smaller for data from WOM15.

While we observe a velocity dispersion profile that is flat within the error bars (Figure 4.6), the data of WOM15 shows a slight increase of the velocity dispersion with radius, even if we exclude stars beyond the tidal radius (Figures 4.8 and 4.10). The difference in the velocity dispersion profiles explains why the recovered DM halo masses are different.

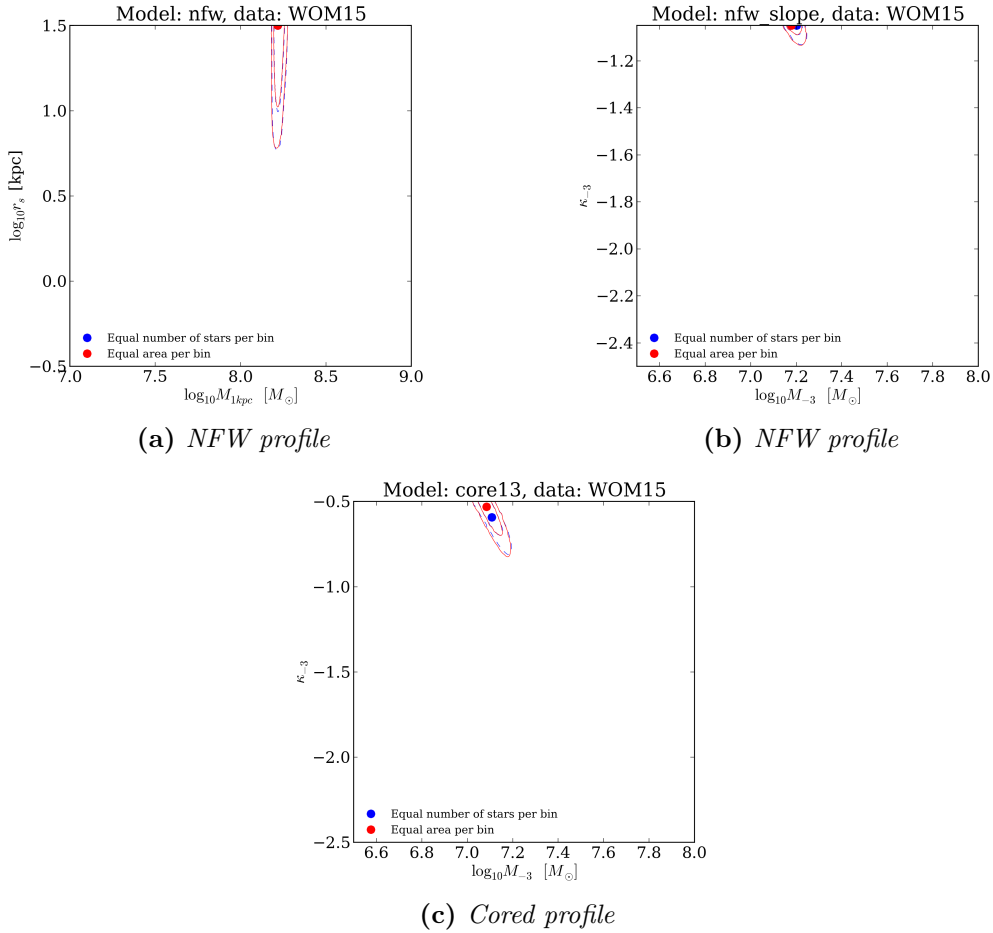
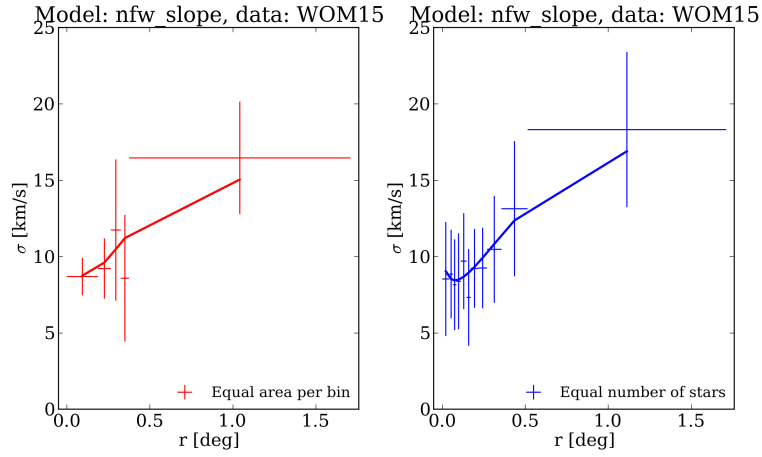
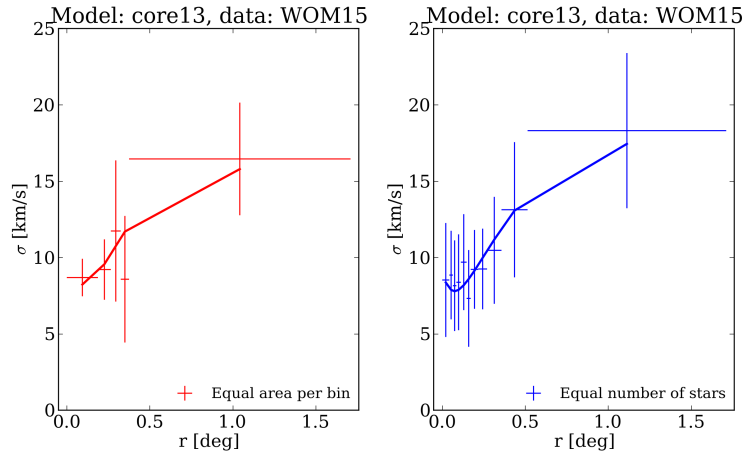


Figure 4.9: Relative likelihood contours for the two parameters κ_{-3} and M_{-3} characterizing the NFW profile (a, b) and the cored profile (c) for WOM15 data including stars beyond a radius of 0.6 degrees. Shown in red and blue are the 1- and 2 σ contours for data using an equal area per bin and an equal number of stars per bin. The highest likelihood is denoted by a dot in the respective color.



(a) NFW profile



(b) Cored profile

Figure 4.10: Modeled LOS velocity dispersion profiles NFW profile (a) and the cored profile (b) for WOM15 data including stars beyond a radius of 0.6 degrees. The colors correspond to the color scheme in Figure 4.7, shown in red and blue are the profiles and data calculated using an equal area per bin and an equal number of stars per bin.

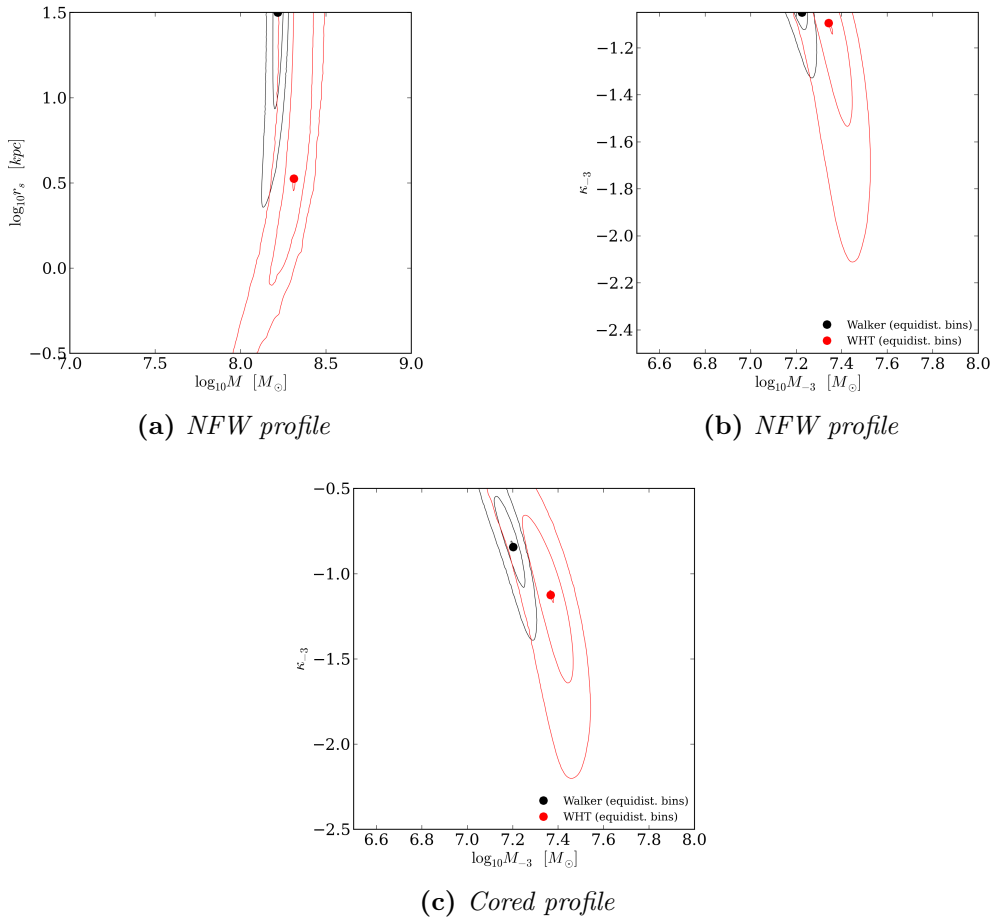


Figure 4.11: Relative likelihood from modeling the WHT (red) and the WOM15 (black) datasets. Shown are the 1 and 2 σ confidence contours and the best-fit parameter values with the highest likelihood for a NFW (a, b) and a cored profile (c).

Chapter 5

Discussion and Conclusion

The aim of this thesis was to use Schwarzschild modeling to model the Local Group dSph galaxy Draco in order to obtain constraints on the nature of its mass profile.

We model data observed by us using the AF2-WYFFOS at the WHT in May 2014 and MMT/Hectochelle data from WOM15, which were described in Chapter 2. Our data shows evidence for a metallicity gradient in Draco, while no such trend could be found in Ursa Minor. The observation of a metallicity gradient has already been reported in previous publications (e.g. Winnick, 2003; Faria et al., 2007). The absence of a gradient in Ursa Minor might be due to its tidal interaction with the MW. Our observed velocities and metallicities are in general in good agreement with those observed by WOM15, however there are still few discrepancies. We suspect that they might be due to faulty sky subtraction in our data reduction.

In Chapter 3 we describe the Schwarzschild method and the main steps of the modeling code developed by Breddels (2013). The dSph galaxies are described using a Plummer profile embedded in a DM halo. We model two parameters describing DM halo profile. We make use of the finding, that there is a radius at which the profile's mass is constrained best. At this radius, all the DM density profiles have a similar logarithmic slope (Breddels et al., 2013). We test the modeling using a Sculptor-like mock galaxy, which has already been used by Breddels (2013) when initially testing the code. We correctly recover the NFW input parameters when using 2000 stars. Since our own datasets are by no means that large, we also randomly select 200 stars to be modeled. This results in elongated contours for the profiles scale parameter (scale radius or logslope). We furthermore corroborate with these tests that there is a radius r_{-3} at which the the best-fit DM profiles have a similar logarithmic slope (Breddels et al., 2013).

In Chapter 4 we describe the results from modeling the two datasets. For both datasets, we find that the stellar component is embedded in an extended DM halo. We recover the mass enclosed within $r_{-3} = 300$ pc. Our best-fit values for the mass agree with findings from Walker et al. (2009), who used Jeans modeling and determined the mass at a similar radius. Their claim, that all dSphs have a similar mass at $r_{300\text{pc}}$ is similar to the proposition of Breddels et al. (2013). From the modeling results of the dSph galaxies Carina, Draco,

Fornax, Leo I, Leo II, Sculptor, Sextans and Ursa Minor, they claim that dSph follow a universal mass profile of the form of a power law.

We furthermore compare the NFW with a cored profile. We find that recovered scale radius of the cored profile is always smaller, which has also been found by Breddels et al. (2013) and Walker et al. (2009), while the enclosed mass is similar, since that leads to a similar slope at r_{-3} . We do not find evidence whether a cored model or a NFW profile is favored. For both models, the recovered velocity dispersion profiles agree with the observed ones and are relatively flat (WHT data) or show an increasing dispersion with radius (WOM15 data).

This thesis is yet another example that the Schwarzschild method is a powerful tool to derive the mass distribution of (dSph) galaxies. Even with our own dataset consisting of 100 stars only, we are able to constrain the mass of the DM halo. With the inclusion of roughly 500 stars from WOM15 stars, we are able to constrain the slope of the dark matter profile much better. The uncertainty of this parameter is driven by the sample size. Eventually, a sample of at least 1000 stars would be desirable. The fact that our best-fit masses agree with the results from Walker et al. (2009), who used a completely different model and a different dataset, provides confidence that the method is working well in our context. It has already been successfully used to derive the mass distribution of four southern dSphs: Fornax, Sculptor, Carina, and Sextans (Breddels et al., 2013).

5.1 Outlook

The data described in this thesis will be re-processed with the improved WEAVE prototype pipeline along with the new observations we took in May 2015. With the re-processed data and a better understanding of the measurement errors, it will be possible to combine our data with the data of WOM15. The observations from May 2015 will provide a number of additional RGB stars that have not been previously observed by us or by WOM15 and a number of stars that are likely LOS-velocity members according to their velocity measurements (WOM15). Furthermore we observed HB stars in Draco, which cover the Mg b region. The increase in the number of observed LOS-velocity members will allow modeling the higher moments of the LOSVD.

To date, there is no spectroscopic survey of the Ursa Minor dSph including LOS velocities, which is available to the public and Ursa Minor has only been modeled using spherical Jeans modeling (Gilmore et al., 2007; Walker et al., 2009). Including the observations from May 2015, the number of stars will be large enough to use Schwarzschild modeling, potentially even using the higher moments of the LOSVD. Further work could also include the use of a Schwarzschild method allowing for axisymmetric or triaxial DM halo potentials.

Bibliography

- Aaronson, M. (1983). “Accurate radial velocities for carbon stars in Draco and Ursa Minor - The first hint of a dwarf spheroidal mass-to-light ratio”. In: *ApJ* 266, pp. L11–L15. DOI: 10.1086/183969.
- Armandroff, T. E., E. W. Olszewski & C. Pryor (1995). “The Mass-To-Light Ratios of the Draco and Ursa Minor Dwarf Spheroidal Galaxies.I. Radial Velocities from Multifiber Spectroscopy”. In: *AJ* 110, p. 2131. DOI: 10.1086/117675.
- Baade, W. (1944a). “NGC 147 and NGC 185, Two New Members of the Local Group of Galaxies”. In: *ApJ* 100, p. 147. DOI: 10.1086/144651.
- (1944b). “The Resolution of Messier 32, NGC 205, and the Central Region of the Andromeda Nebula.” In: *ApJ* 100, p. 137. DOI: 10.1086/144650.
- Baade, W. & H. H. Swope (1961). “The Draco system, a dwarf galaxy.” In: *AJ* 66, pp. 300–347. DOI: 10.1086/108431.
- Battaglia, G. et al. (2008a). “Analysis and calibration of CaII triplet spectroscopy of red giant branch stars from VLT/FLAMES observations”. In: *MNRAS* 383, pp. 183–199. DOI: 10.1111/j.1365-2966.2007.12532.x. arXiv: 0710.0798.
- Battaglia, G. et al. (2008b). “The Kinematic Status and Mass Content of the Sculptor Dwarf Spheroidal Galaxy”. In: *ApJ* 681, pp. L13–L16. DOI: 10.1086/590179. arXiv: 0802.4220.
- Belokurov, V. et al. (2006). “A Faint New Milky Way Satellite in Bootes”. In: *ApJ* 647, pp. L111–L114. DOI: 10.1086/507324. eprint: astro-ph/0604355.
- Belokurov, V. et al. (2007). “Cats and Dogs, Hair and a Hero: A Quintet of New Milky Way Companions”. In: *ApJ* 654, pp. 897–906. DOI: 10.1086/509718. eprint: astro-ph/0608448.
- Benson, A. J. et al. (2002a). “The effects of photoionization on galaxy formation - I. Model and results at $z=0$ ”. In: *MNRAS* 333, pp. 156–176. DOI: 10.1046/j.1365-8711.2002.05387.x. eprint: astro-ph/0108217.
- Benson, A. J. et al. (2002b). “The effects of photoionization on galaxy formation - II. Satellite galaxies in the Local Group”. In: *MNRAS* 333, pp. 177–190. DOI: 10.1046/j.1365-8711.2002.05388.x. eprint: astro-ph/0108218.
- Binnewies, S. & J. Pöpsel (2015). *Capella Observatory*. <http://www.capella-observatory.com/ImageHTMLs/Galaxies/UMiDwarf.htm>. Online; accessed 27-05-2015.

-
- Binney, J. & S. Tremaine (2008). *Galactic Dynamics: Second Edition*. Princeton University Press.
- Breddels, M. A. & A. Helmi (2013). “Model comparison of the dark matter profiles of Fornax, Sculptor, Carina and Sextans”. In: *A&A* 558, A35, A35. DOI: 10.1051/0004-6361/201321606. arXiv: 1304.2976.
- Breddels, M. A. et al. (2013). “Orbit-based dynamical models of the Sculptor dSph galaxy”. In: *MNRAS* 433, pp. 3173–3189. DOI: 10.1093/mnras/stt956. arXiv: 1205.4712 [astro-ph.CO].
- Breddels, Maarten Adriaan (2013). “Orbit-based dynamical models of Local Group dwarf spheroidal galaxies”. Relation: <http://www.rug.nl/> Rights: University of Groningen. PhD thesis. University of Groningen. ISBN: 9789036763035.
- Canterna, R. & R. A. Schommer (1978). “The chemical abundances of extreme population II systems.” In: *ApJ* 219, pp. L119–L123. DOI: 10.1086/182620.
- Cole, S. et al. (1994). “A Recipe for Galaxy Formation”. In: *MNRAS* 271, p. 781. eprint: astro-ph/9402001.
- Cretton, N. et al. (1999). “Axisymmetric Three-Integral Models for Galaxies”. In: *ApJS* 124, pp. 383–401. DOI: 10.1086/313264. eprint: astro-ph/9902034.
- de Blok, W. J. G. (2010). “The Core-Cusp Problem”. In: *Advances in Astronomy* 2010, 789293, p. 5. DOI: 10.1155/2010/789293. arXiv: 0910.3538.
- De Lucia, G. & A. Helmi (2008). “The Galaxy and its stellar halo: insights on their formation from a hybrid cosmological approach”. In: *MNRAS* 391, pp. 14–31. DOI: 10.1111/j.1365-2966.2008.13862.x. arXiv: 0804.2465.
- Dehnen, W. (1993). “A Family of Potential-Density Pairs for Spherical Galaxies and Bulges”. In: *MNRAS* 265, p. 250.
- Dolphin, A. E. (2002). “Numerical methods of star formation history measurement and applications to seven dwarf spheroidals”. In: *MNRAS* 332, pp. 91–108. DOI: 10.1046/j.1365-8711.2002.05271.x. eprint: astro-ph/0112331.
- Einasto, J. et al. (1974). “Missing mass around galaxies - Morphological evidence”. In: *Nature* 252, pp. 111–113. DOI: 10.1038/252111a0.
- Faber, S. M. & D. N. C. Lin (1983). “Is there nonluminous matter in dwarf spheroidal galaxies”. In: *ApJ* 266, pp. L17–L20. DOI: 10.1086/183970.
- Faria, D. et al. (2007). “The usage of Strömberg photometry in studies of local group dwarf spheroidal galaxies. Application to Draco: a new catalogue of Draco members and a study of the metallicity distribution function and radial gradients”. In: *A&A* 465, pp. 357–373. DOI: 10.1051/0004-6361:20065244. eprint: astro-ph/0611883.
- Gilmore, G. et al. (2007). “Observed Properties of Dark Matter: dynamical studies of dSph galaxies”. In: *Nuclear Physics B Proceedings Supplements* 173, pp. 15–18. DOI: 10.1016/j.nuclphysbps.2007.08.143. eprint: astro-ph/0608528.
- Grillmair, C. J. et al. (1998). “Hubble Space Telescope observations of the Draco dwarf spheroidal galaxy”. In: *AJ* 115, p. 144. DOI: 10.1086/300169. eprint: astro-ph/9709259.

-
- Hodge, P. W. & R. W. Michie (1969). “The Structure of Dwarf Elliptical Galaxies of the Local Group”. In: *AJ* 74, p. 587. DOI: 10.1086/110840.
- Illingworth, G. (1976). “The masses of globular clusters. II - Velocity dispersions and mass-to-light ratios”. In: *ApJ* 204, pp. 73–93. DOI: 10.1086/154152.
- Irwin, M. & D. Hatzidimitriou (1995). “Structural parameters for the Galactic dwarf spheroidals”. In: *MNRAS* 277, pp. 1354–1378.
- Isaac Newton Group of Telescopes (2012). *Autofib 2*. http://www.ing.iac.es/PR/wht_info/whtauto.html.
- Jardel, J. R. & K. Gebhardt (2012). “The Dark Matter Density Profile of the Fornax Dwarf”. In: *ApJ* 746, 89, p. 89. DOI: 10.1088/0004-637X/746/1/89. arXiv: 1112.0319.
- Jardel, J. R. et al. (2013). “Measuring Dark Matter Profiles Non-Parametrically in Dwarf Spheroidals: An Application to Draco”. In: *ApJ* 763, 91, p. 91. DOI: 10.1088/0004-637X/763/2/91. arXiv: 1211.5376 [astro-ph.CO].
- King, I. (1962). “The structure of star clusters. I. an empirical density law”. In: *AJ* 67, p. 471. DOI: 10.1086/108756.
- King, I. R. (1966). “The structure of star clusters. III. Some simple dynamical models”. In: *AJ* 71, p. 64. DOI: 10.1086/109857.
- Klessen, R. S., E. K. Grebel & D. Harbeck (2003). “Draco: A Failure of the Tidal Model”. In: *ApJ* 589, pp. 798–809. DOI: 10.1086/374816. eprint: astro-ph/0302287.
- Kleyna, J. T. et al. (1998). “A V and I CCD Mosaic Survey of the Ursa Minor Dwarf Spheroidal Galaxy”. In: *AJ* 115, pp. 2359–2368. DOI: 10.1086/300360.
- Kleyna, J. T. et al. (2001). “First Clear Signature of an Extended Dark Matter Halo in the Draco Dwarf Spheroidal”. In: *ApJ* 563, pp. L115–L118. DOI: 10.1086/338603. eprint: astro-ph/0111329.
- (2005). “Ursa Major: A Missing Low-Mass CDM Halo?” In: *ApJ* 630, pp. L141–L144. DOI: 10.1086/491654. eprint: astro-ph/0507154.
- Klypin, A. et al. (1999). “Where Are the Missing Galactic Satellites?” In: *ApJ* 522, pp. 82–92. DOI: 10.1086/307643. eprint: astro-ph/9901240.
- Koposov, S. E. et al. (2015). “Beasts of the Southern Wild : Discovery of nine Ultra Faint satellites in the vicinity of the Magellanic Clouds.” In: *ApJ* 805, 130, p. 130. DOI: 10.1088/0004-637X/805/2/130. arXiv: 1503.02079.
- Lokas, Ewa L. (2001). “Velocity dispersions of dwarf spheroidal galaxies: dark matter versus MOND”. In: *Monthly Notices of the Royal Astronomical Society* 327.2, pp. L21–L26. DOI: 10.1046/j.1365-8711.2001.04953.x. eprint: <http://mnras.oxfordjournals.org/content/327/2/L21.full.pdf+html>. URL: <http://mnras.oxfordjournals.org/content/327/2/L21.abstract>.
- Martínez-Delgado, D. et al. (2001). “A Tidal Extension in the Ursa Minor Dwarf Spheroidal Galaxy”. In: *ApJ* 549, pp. L63–L66. DOI: 10.1086/319150. eprint: astro-ph/0101456.
- Mateo, M. L. (1998). “Dwarf Galaxies of the Local Group”. In: *ARA&A* 36, pp. 435–506. DOI: 10.1146/annurev.astro.36.1.435. eprint: astro-ph/9810070.

-
- Mayer, L. et al. (2001). “Tidal Stirring and the Origin of Dwarf Spheroidals in the Local Group”. In: *ApJ* 547, pp. L123–L127. DOI: 10.1086/318898. eprint: astro-ph/0011041.
- Mayer, L. et al. (2006). “Simultaneous ram pressure and tidal stripping; how dwarf spheroidals lost their gas”. In: *MNRAS* 369, pp. 1021–1038. DOI: 10.1111/j.1365-2966.2006.10403.x. eprint: astro-ph/0504277.
- McConnachie, A. W. (2012). “The Observed Properties of Dwarf Galaxies in and around the Local Group”. In: *AJ* 144, 4, p. 4. DOI: 10.1088/0004-6256/144/1/4. arXiv: 1204.1562 [astro-ph.CO].
- Moore, B. et al. (1999). “Dark Matter Substructure within Galactic Halos”. In: *ApJ* 524, pp. L19–L22. DOI: 10.1086/312287. eprint: astro-ph/9907411.
- Moore, J. (2015). *Farnham Astronomical Society*. <http://www.farnham-as.co.uk/2009/09/the-draco-dwarf-galaxy-ugc-10822-imaged-by-john-moore/>. Online; accessed 27-05-2015.
- Muñoz, R. R. et al. (2012). “The Discovery of an Ultra-faint Star Cluster in the Constellation of Ursa Minor”. In: *ApJ* 753, L15, p. L15. DOI: 10.1088/2041-8205/753/1/L15. arXiv: 1204.5750.
- Navarro, J. F., V. R. Eke & C. S. Frenk (1996). “The cores of dwarf galaxy haloes”. In: *MNRAS* 283, pp. L72–L78. eprint: astro-ph/9610187.
- Navarro, J. F., C. S. Frenk & S. D. M. White (1996). “The Structure of Cold Dark Matter Halos”. In: *ApJ* 462, p. 563. DOI: 10.1086/177173. eprint: arXiv:astro-ph/9508025.
- (1997). “A Universal Density Profile from Hierarchical Clustering”. In: *ApJ* 490, pp. 493–508. eprint: astro-ph/9611107.
- Odenkirchen, M. et al. (2001). “New Insights on the Draco Dwarf Spheroidal Galaxy from the Sloan Digital Sky Survey: A Larger Radius and No Tidal Tails”. In: *AJ* 122, pp. 2538–2553. DOI: 10.1086/323715. eprint: astro-ph/0108100.
- Olszewski, E. W. & M. Aaronson (1985). “The URSA Minor dwarf galaxy - Still an old stellar system”. In: *AJ* 90, pp. 2221–2238. DOI: 10.1086/113925.
- Peñarrubia, J. et al. (2012). “The Coupling between the Core/Cusp and Missing Satellite Problems”. In: *ApJ* 759, L42, p. L42. DOI: 10.1088/2041-8205/759/2/L42. arXiv: 1207.2772 [astro-ph.GA].
- Peebles, P. J. E. (1982). “Primeval adiabatic perturbations - Effect of massive neutrinos”. In: *ApJ* 258, pp. 415–424. DOI: 10.1086/160094.
- Piatek, S. et al. (2002). “Structure of the Draco Dwarf Spheroidal Galaxy”. In: *AJ* 123, pp. 2511–2524. DOI: 10.1086/339698. eprint: astro-ph/0201297.
- Planck Collaboration et al. (2014). “Planck 2013 results. XVI. Cosmological parameters”. In: *A&A* 571, A16, A16. DOI: 10.1051/0004-6361/201321591. arXiv: 1303.5076 [astro-ph.CO].
- Plummer, H. C. (1911). “On the problem of distribution in globular star clusters”. In: *MNRAS* 71, pp. 460–470.

-
- Powell, R. (2015). *An Atlas of the Universe*. <http://www.atlasoftheuniverse.com/>. Online; accessed 27-05-2015.
- Revaz, Y. & P. Jablonka (2012). “The dynamical and chemical evolution of dwarf spheroidal galaxies with GEAR”. In: *A&A* 538, A82, A82. DOI: 10.1051/0004-6361/201117402. arXiv: 1109.0989.
- Revaz, Y. et al. (2009). “The dynamical and chemical evolution of dwarf spheroidal galaxies”. In: *A&A* 501, pp. 189–206. DOI: 10.1051/0004-6361/200911734. arXiv: 0904.4636.
- Richstone, D. O. & S. Tremaine (1984). “A general method for constructing spherical galaxy models”. In: *ApJ* 286, pp. 27–37. DOI: 10.1086/162572.
- (1986). “Measuring mass-to-light ratios of spherical stellar systems by core fitting”. In: *AJ* 92, pp. 72–74. DOI: 10.1086/114135.
- Rix, H.-W. et al. (1997). “Dynamical Modeling of Velocity Profiles: The Dark Halo around the Elliptical Galaxy NGC 2434”. In: *ApJ* 488, pp. 702–719. eprint: astro-ph/9702126.
- Rood, H. J. et al. (1972). “The Structure of the Coma Cluster of Galaxies”. In: *ApJ* 175, p. 627. DOI: 10.1086/151585.
- Salvadori, S., R. Schneider & A. Ferrara (2007). “Cosmic stellar relics in the Galactic halo”. In: *MNRAS* 381, pp. 647–662. DOI: 10.1111/j.1365-2966.2007.12133.x. eprint: astro-ph/0611130.
- Schwarzschild, M. (1979). “A numerical model for a triaxial stellar system in dynamical equilibrium”. In: *ApJ* 232, pp. 236–247. DOI: 10.1086/157282.
- Ségall, M. et al. (2007). “Draco, a flawless dwarf galaxy”. In: *MNRAS* 375, pp. 831–842. DOI: 10.1111/j.1365-2966.2006.11356.x. eprint: astro-ph/0612263.
- Shapley, H. (1938). “Two Stellar Systems of a New Kind”. In: *Nature* 142, pp. 715–716. DOI: 10.1038/142715b0.
- Shetrone, M. D., M. Bolte & P. B. Stetson (1998). “Keck HIRES Abundances in the Dwarf Spheroidal Galaxy Draco”. In: *AJ* 115, pp. 1888–1893. DOI: 10.1086/300341.
- Shetrone, M. D., P. Côté & W. L. W. Sargent (2001). “Abundance Patterns in the Draco, Sextans, and Ursa Minor Dwarf Spheroidal Galaxies”. In: *ApJ* 548, pp. 592–608. DOI: 10.1086/319022. eprint: astro-ph/0009505.
- Somerville, R. S. & J. R. Primack (1999). “Semi-analytic modelling of galaxy formation: the local Universe”. In: *MNRAS* 310, pp. 1087–1110. DOI: 10.1046/j.1365-8711.1999.03032.x. eprint: astro-ph/9802268.
- Starkenburger, E. et al. (2010). “The NIR Ca ii triplet at low metallicity. Searching for extremely low-metallicity stars in classical dwarf galaxies”. In: *A&A* 513, A34, A34. DOI: 10.1051/0004-6361/200913759. arXiv: 1002.2963 [astro-ph.SR].
- Starkenburger, E. et al. (2013). “The satellites of the Milky Way - insights from semi-analytic modelling in a Λ CDM cosmology”. In: *MNRAS* 429, pp. 725–743. DOI: 10.1093/mnras/sts367. arXiv: 1206.0020.

-
- Tolstoy, E., V. Hill & M. Tosi (2009). “Star-Formation Histories, Abundances, and Kinematics of Dwarf Galaxies in the Local Group”. In: *ARA&A* 47, pp. 371–425. DOI: 10.1146/annurev-astro-082708-101650. arXiv: 0904.4505 [astro-ph.CO].
- van den Bergh, S. (1999). “Subclustering among Local Group Galaxies”. In: *AJ* 117, pp. 2211–2212. DOI: 10.1086/300861. eprint: astro-ph/9902296.
- van den Bosch, R. C. E. et al. (2008). “Triaxial orbit based galaxy models with an application to the (apparent) decoupled core galaxy NGC 4365”. In: *MNRAS* 385, pp. 647–666. DOI: 10.1111/j.1365-2966.2008.12874.x. arXiv: 0712.0113.
- Walker, M. (2013). “Dark Matter in the Galactic Dwarf Spheroidal Satellites”. In: *Planets, Stars and Stellar Systems. Volume 5: Galactic Structure and Stellar Populations*. Oswald, T. D. and Gilmore, G., p. 1039. DOI: 10.1007/978-94-007-5612-0_20.
- Walker, M. G., E. W. Olszewski & M. Mateo (2015). “Bayesian analysis of resolved stellar spectra: application to MMT/Hectochelle observations of the Draco dwarf spheroidal”. In: *MNRAS* 448, pp. 2717–2732. DOI: 10.1093/mnras/stv099. arXiv: 1503.02589.
- Walker, M. G. et al. (2007). “Velocity Dispersion Profiles of Seven Dwarf Spheroidal Galaxies”. In: *ApJ* 667, pp. L53–L56. DOI: 10.1086/521998. arXiv: 0708.0010.
- Walker, M. G. et al. (2009). “A Universal Mass Profile for Dwarf Spheroidal Galaxies?” In: *ApJ* 704, pp. 1274–1287. DOI: 10.1088/0004-637X/704/2/1274. arXiv: 0906.0341 [astro-ph.CO].
- Walsh, S. M., H. Jerjen & B. Willman (2007). “A Pair of Boötes: A New Milky Way Satellite”. In: *ApJ* 662, pp. L83–L86. DOI: 10.1086/519684. arXiv: 0705.1378.
- Weisz, D. R. et al. (2011). “How Typical Are the Local Group Dwarf Galaxies?” In: *ApJ* 743, 8, p. 8. DOI: 10.1088/0004-637X/743/1/8. arXiv: 1101.1301.
- Weisz, D. R. et al. (2014). “The Star Formation Histories of Local Group Dwarf Galaxies. I. Hubble Space Telescope/Wide Field Planetary Camera 2 Observations”. In: *ApJ* 789, 147, p. 147. DOI: 10.1088/0004-637X/789/2/147. arXiv: 1404.7144.
- White, S. D. M. & M. J. Rees (1978). “Core condensation in heavy halos - A two-stage theory for galaxy formation and clustering”. In: *MNRAS* 183, pp. 341–358.
- Willman, B. et al. (2005a). “A New Milky Way Companion: Unusual Globular Cluster or Extreme Dwarf Satellite?” In: *AJ* 129, pp. 2692–2700. DOI: 10.1086/430214. eprint: astro-ph/0410416.
- Willman, B. et al. (2005b). “A New Milky Way Dwarf Galaxy in Ursa Major”. In: *ApJ* 626, pp. L85–L88. DOI: 10.1086/431760. eprint: astro-ph/0503552.
- Wilson, A. G. (1955). “Sculptor-Type Systems in the Local Group of Galaxies”. In: *PASP* 67, pp. 27–29. DOI: 10.1086/126754.
- Winnick, R. A. (2003). “Metallicity distributions in the Draco, Ursa Minor and Sculptor dwarf spheroidal galaxies”. PhD thesis. Yale University.
- Wolf, J. et al. (2010). “Accurate masses for dispersion-supported galaxies”. In: *MNRAS* 406, pp. 1220–1237. DOI: 10.1111/j.1365-2966.2010.16753.x. arXiv: 0908.2995.
- Zinn, R. (1978). “The metal abundance range in the Draco dwarf galaxy”. In: *ApJ* 225, pp. 790–803. DOI: 10.1086/156544.

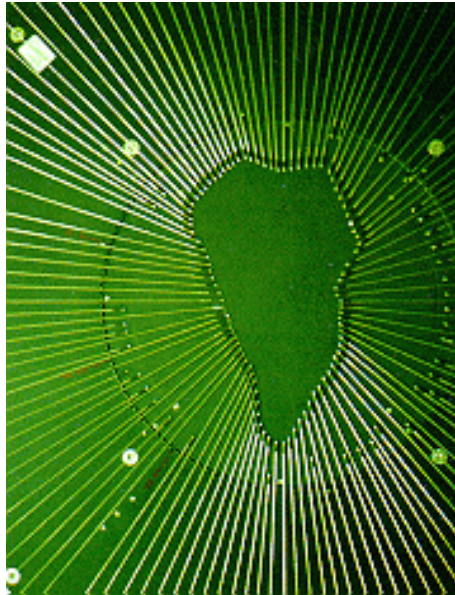
-
- Zinn, R. (1981). “The metal abundance range in the Ursa Minor dwarf galaxy”. In: *ApJ* 251, pp. 52–60. DOI: 10.1086/159440.
- Zucker, D. B. et al. (2006a). “A Curious Milky Way Satellite in Ursa Major”. In: *ApJ* 650, pp. L41–L44. DOI: 10.1086/508628. eprint: astro-ph/0606633.
- Zucker, D. B. et al. (2006b). “A New Milky Way Dwarf Satellite in Canes Venatici”. In: *ApJ* 643, pp. L103–L106. DOI: 10.1086/505216. eprint: astro-ph/0604354.
- Zwicky, F. (1937). “On the Masses of Nebulae and of Clusters of Nebulae”. In: *ApJ* 86, p. 217. DOI: 10.1086/143864.

Acknowledgements

First of all, this thesis would not have been possible without my great supervisors. Eline, thank you for supervising me! Thank you for your patience, your knowledge, your support, your suggestions, and of course also for giving me opportunity to go observing to La Palma! Shoko, thank you for all your help, guidance and encouragement throughout this project. I am really grateful for the feedback I got from you. Maarten, thank you for letting me use your code and for all the help and suggestions. Amina, thank you for your useful suggestions and your guidance during my time in Groningen. I would also like to extend my thanks to Scott and Peter, who agreed to be on my thesis committee.

Dear secretaries, thank you very much for your help and patience, especially during the organization of the La Palma trip! I am also grateful to the support of the computer group, which helped me out a number of times.

A big thanks to all the Astronomy students at the Kapteyn Institute, especially the 'inhabitants' of room 193. I really enjoyed my time here! Marten, thanks for being such a great house/office/choir-mate and friend. Jorien, thank you for everything, I will miss you! Jorrit, thank you for the useful discussions and help. Ilham, thank you for all the nice tea breaks we had together! My thanks extend to my friends and family outside of the Kapteyn Institute, who made sure that I do not spend all my time with my thesis. I furthermore greatly acknowledge support from the Studienstiftung des deutschen Volkes.



Fibers of AF2/WYFFOS positioned to outline the shape of La Palma (Isaac Newton Group of Telescopes, 2012).

List of Figures

1.1	Galaxies in the Local Group (left) and a zoom-in of the satellite-galaxy system of the MW (right, Powell (2015)).	6
1.2	Image of the Draco dSph (Moore, 2015).	7
1.3	Image of the Ursa Minor dSph (Binnewies & Pöpsel, 2015).	8
2.1	CMDs of the Draco (left) and the Ursa Minor (right) dSphs within their ditdal radius. The candidate RGB stars to be observed are shown in red and HB stars are shown in blue.	13
2.2	Metallicity versus heliocentric LOS velocity color coded by S/N per Å of Draco (left) and Ursa Minor (right) and PDF of the LOS velocity. The membership regions are shaded in red and all stars outside this region are most likely non-members.	14
2.3	Spatial distribution of likely velocity member stars in Draco (left) and Ursa Minor (right) with S/N per Å ≤ 12 . The stars are color-coded by their heliocentric LOS velocity.	14
2.4	Elliptical radius versus metallicity for the Draco (left) and Ursa Minor (right) dSphs.	15
2.5	Spatial distribution of likely velocity member stars in Draco (left) and Ursa Minor (right) with S/N per Å ≤ 12 . The stars are color-coded by their metallicity.	15
2.6	Comparison of the LOS velocities of stars present in our Draco data and published by WOM15. The right panel shows the likely velocity members.	16
2.7	Comparison of the [Fe/H] values of likely velocity member stars present in our Draco data and published by WOM15.	17
3.1	Relative likelihood contours for the two parameters κ_{-3} and M_{-3} characterizing the NFW profile (a, b) and the cored profile (c) for a Sculptor-like mock galaxy. The free parameters in (a) are the $M_{1\text{kpc}}$ and r_s and in (b) and (c) they are M_{-3} and κ_{-3} . Shown in black and red are the 1- and 2σ contours for datasets consisting of 2000 and 200 stars respectively, using equidistant binning. The highest likelihood is denoted by a dot in the respective color.	26

4.1	Spatial distribution of stars in Draco observed by us (WHT) Shown in red are the two radial bins for (from left to right) equidistant binning, bins containing the same number of stars, and bins covering the same area. . . .	28
4.2	Histograms of the star counts of the bins presented in Figure 4.1. Shown from left to right are the two radial bins for equidistant binning, bins containing the same number of stars, and bins covering the same area.	28
4.3	Spatial distribution of stars in Draco observed by WOM15. The top row shows the bins which cover the data in the same radial range as ours and the bottom row the full data range. Shown from left to right are the two radial bins for equidistant binning, bins containing the same number of stars, and bins covering the same area.	29
4.4	Histograms of the radius versus the number of stars in each bin. From top left to bottom right: Our data with equidistant bins, WOM15 data in the same radial range and the same bins, WOM15's data in the same radial range with bins containing ~ 50 stars, and Walker's data in the full radial range with bins containing ~ 50 stars.	30
4.5	Relative likelihood contours for the two parameters κ_{-3} and M_{-3} characterizing the NFW profile (a) and the cored profile (b) for WHT data. Shown in black (red, blue) are the 1- and 2σ contours for data using equidistant bins (an equal area per bin, an equal number of stars per bin). The highest likelihood is denoted by a dot in the respective color.	32
4.6	Modeled LOS velocity dispersion profiles NFW profile (a, b) and the cored profile (c) for WHT data. The colors correspond to the color scheme in Figure 4.5. The errorbars are the binned velocity dispersion profiles obtained from the data. The width of the error bar indicates the radial bin width. . .	33
4.7	Relative likelihood contours for the two parameters κ_{-3} and M_{-3} characterizing the NFW profile (a, b) and the cored profile (c) for WOM15 data within a radius of 0.6 degrees. Shown in black (red, blue) are the 1- and 2σ contours for data using equidistant bins (an equal area per bin, an equal number of stars per bin). The highest likelihood is denoted by a dot in the respective color.	35
4.8	Modeled LOS velocity dispersion profiles NFW profile (a) and the cored profile (b) for WOM15 data within a radius of 0.6 degrees. The colors correspond to the color scheme in Figure 4.7, shown in black (red, blue) are the profiles and data calculated using equidistant bins (an equal area per bin, an equal number of stars per bin).	36

4.9	Relative likelihood contours for the two parameters κ_{-3} and M_{-3} characterizing the NFW profile (a, b) and the cored profile (c) for WOM15 data including stars beyond a radius of 0.6 degrees. Shown in red and blue are the 1- and 2σ contours for data using an equal area per bin and an equal number of stars per bin. The highest likelihood is denoted by a dot in the respective color.	37
4.10	Modeled LOS velocity dispersion profiles NFW profile (a) and the cored profile (b) for WOM15 data including stars beyond a radius of 0.6 degrees. The colors correspond to the color scheme in Figure 4.7, shown in red and blue are the profiles and data calculated using an equal area per bin and an equal number of stars per bin.	38
4.11	Relative likelihood from modeling the WHT (red) and the WOM15 (black) datasets. Shown are the 1 and 2σ confidence contours and the best-fit parameter values with the highest likelihood for a NFW (a, b) and a cored profile (c).	39

List of Tables

- 4.1 Best-fit results for the free parameters of the NFW and cored profiles. The left column indicates which dataset was used. The number in brackets behind WHT corresponds to the binning routine used (cf. Section 4.1.2). . 34
- 4.2 Best-fit results for the free parameters of the NFW and cored profiles. The left column indicates which dataset was used. The number in brackets behind WOM15 corresponds to the binning routine used (cf. Section 4.1.2). The results in the top half of the table were obtained using data within a radius of 0.6 degrees and the results in the bottom half using the full dataset. 34

Acronyms

AF2 AutoFib2

CDM cold dark matter

CMD color-magnitude diagram

dE dwarf elliptical

DF distribution function

dIrr dwarf irregular

DM dark matter

dSph dwarf spheroidal

[Fe/H] metallicity

LOS line-of-sight

LOSVD line-of-sight velocity distribution

M31 Andromeda galaxy

M/L mass-to-light ratio

MMT Multiple Mirror Telescope

MW Milky Way

NFW Navarro, Frenck, & White

QP quadratic programming

RGB red giant branch

S/N per Å signal-to-noise ratio per Ångström

WHT William Herschel Telescope

WYFFOS Wide Field Fibre Optical Spectrograph

Appendix A

Jeans modeling

In a collisionless system, stars can be treated as tracer objects moving on orbits in a potential field due to a smooth mass distribution. If that was not the case, we would have to treat the stars as a collection of massive points. A dSph galaxy can be treated as a collisionless system, since its relaxation time is much larger than the crossing time, which is the time needed for a typical star to cross the galaxy. The relaxation time is the time after which the many encounters with other stars have changed the star's orbit so much that its initial conditions cannot be recovered assuming a smooth mass distribution.

The system can be described by a distribution function (DF) $f(\mathbf{x}, \mathbf{v}, t)$. The probability of finding a star in the 6D phase-space volume $d^3\mathbf{x} d^3\mathbf{v}$ at time t is $f(\mathbf{x}, \mathbf{v}, t) d^3\mathbf{x} d^3\mathbf{v}$. Since it is a probability, f is normalized as follows:

$$\int f(\mathbf{x}, \mathbf{v}, t) d^3\mathbf{x} d^3\mathbf{v} = 1 \quad (\text{A.1})$$

Similar to the conservation of mass in a fluid flow, which is described by the continuity equation

$$\frac{\partial \rho}{\partial t} + \frac{\partial}{\partial \mathbf{x}} \cdot (\rho \dot{\mathbf{x}}) = 0, \quad (\text{A.2})$$

the probability in phase space $\mathbf{w} = (\mathbf{q}, \mathbf{p})$ has to be conserved as the DF f evolves:

$$\frac{\partial f}{\partial t} + \frac{\partial}{\partial \mathbf{w}} \cdot (f \dot{\mathbf{w}}) = 0 \quad (\text{A.3})$$

Using Hamilton's equations $\dot{\mathbf{q}} = \partial H / \partial \mathbf{p}$ and $\dot{\mathbf{p}} = -\partial H / \partial \mathbf{q}$, $\dot{\mathbf{w}} = (\dot{\mathbf{q}}, \dot{\mathbf{p}})$ can be eliminated and the **collisionless Boltzmann equation** (CBE) is obtained:

$$\frac{\partial f}{\partial t} + \dot{\mathbf{q}} \cdot \frac{\partial f}{\partial \mathbf{q}} + \dot{\mathbf{p}} \cdot \frac{\partial f}{\partial \mathbf{p}} = 0 \quad (\text{A.4})$$

In inertial Cartesian coordinates (\mathbf{x}, \mathbf{v}) , the Hamiltonian is $H = v^2/2 + \Phi(\mathbf{x}, t)$, and the CBE becomes

$$\frac{\partial f}{\partial t} + \mathbf{v} \cdot \frac{\partial f}{\partial \mathbf{x}} - \frac{\partial \Phi}{\partial \mathbf{x}} \cdot \frac{\partial f}{\partial \mathbf{v}} = 0. \quad (\text{A.5})$$

The CBE describes the flow of a probability “fluid” through phase space. The flow is incompressible, since the phase-space density f around a given star is constant. This, however, does not imply that the phase-space density around all stars is the same.

Integrating equation (A.5) over all velocities gives

$$\int d^3\mathbf{v} \frac{\partial f}{\partial t} + \int d^3\mathbf{v} v_i \frac{\partial f}{\partial x_i} - \frac{\partial \Phi}{\partial x_i} \int d^3\mathbf{v} \frac{\partial f}{\partial v_i} = 0 \quad (\text{A.6})$$

using the summation convention, summing over i . In the following, we use the density, defined as

$$\nu(\mathbf{x}) \equiv \int d^3\mathbf{v} f(\mathbf{x}, \mathbf{v}), \quad (\text{A.7})$$

and the mean velocity, defined as

$$\bar{\mathbf{v}} \equiv \frac{1}{\nu(\mathbf{x})} \int d^3\mathbf{v} \mathbf{v} f(\mathbf{x}, \mathbf{v}). \quad (\text{A.8})$$

The last term of equation (A.6) can be dropped since

$$\begin{aligned} \frac{\partial \Phi}{\partial x_i} \int d^3\mathbf{v} \frac{\partial f}{\partial v_i} &= \sum_i \int d^3\mathbf{v} \frac{\partial f}{\partial v_i} \frac{\partial \Phi}{\partial x_i} \int d^3\mathbf{v} \frac{\partial f}{\partial v_i} = \int d^3\mathbf{v} \nabla_x \Phi \cdot \nabla_v f \\ &= \int f d\mathbf{S} \cdot \nabla_x \Phi - \int d^3\mathbf{v} f \nabla_x \cdot \nabla_v \Phi = 0. \end{aligned} \quad (\text{A.9})$$

first applying the divergence theorem. The first term is zero under the assumption that $f(\mathbf{x}, \mathbf{v}, t) = 0$ for large $|\mathbf{v}|$. Due to the choice of coordinate system, $\nabla_x \cdot \nabla_v = 0$. Thus equation (A.6) simplifies to

$$\frac{\partial \nu}{\partial t} + \frac{\partial(\nu \bar{v}_i)}{\partial x_i} = 0, \quad (\text{A.10})$$

which is the continuity equation for stellar systems.

Equation (A.5) is multiplied by the velocity moment v_j and integrated over all velocities again:

$$\int d^3\mathbf{v} v_j \frac{\partial f}{\partial t} + \int d^3\mathbf{v} v_i v_j \frac{\partial f}{\partial x_i} - \frac{\partial \Phi}{\partial x_i} \int d^3\mathbf{v} v_j \frac{\partial f}{\partial v_i} = 0 \quad (\text{A.11})$$

Using partial integration and equations (A.7) and (A.8), the equation above simplifies to

$$\frac{\partial(\nu v_j)}{\partial t} + \frac{\partial(\nu \bar{v}_i v_j)}{\partial x_i} + \nu \frac{\partial \Phi}{\partial x_j} = 0. \quad (\text{A.12})$$

After subtracting equation (A.10) multiplied by v_j from the equation above, an analog of Euler's equation of fluid flow is obtained

$$\nu \frac{\partial \bar{v}_j}{\partial t} + \nu \bar{v}_i \frac{\partial \bar{v}_j}{\partial v_i} = -\nu \frac{\partial \Phi}{\partial x_j} - \frac{\partial(\nu \sigma_{ij}^2)}{\partial x_i}, \quad (\text{A.13})$$

where σ_{ij}^2 is the velocity dispersion tensor defined as

$$\begin{aligned} \sigma_{ij}^2 &\equiv \frac{1}{\nu(\mathbf{x})} \int d^3 \mathbf{v} (v_i - \bar{v}_i)(v_j - \bar{v}_j) f(\mathbf{x}, \mathbf{v}) \\ &= \overline{v_i v_j} - \bar{v}_i \bar{v}_j. \end{aligned} \quad (\text{A.14})$$

Equations (A.10) and (A.13) are known as **Jeans equations**, since they were first applied to stellar dynamics by Jeans in 1919.